

The Development of a UFS-Boyden Photometric Pipeline to Facilitate the Observational Study of Accretion Driven Systems

Johannes Jacobus Calitz

*This thesis is submitted as partial fulfillment of the requirements
for the qualification*

Magister Scientiae

in the

Faculty of Natural and Agricultural Sciences

Department of Physics

University of the Free State

Supervisor : Prof. P.J. Meintjes

Date of submission : 2005/05/30

Acknowledgements

I would like to thank prof. P.J. Meintjes for his assistance, guidance, ideas and chats, during the few years it took to finish this study. Many thanks goes to Dr. M.J.H. Hoffman for his ideas and insights into certain problematic aspects of the observing, and pointing out some bugs in the developed software.

To my wife and kids, who endured many frustrating hours with an absent dad in the house, thank you very much!

I am very grateful for the NRF for financial support during the first two years of study.

To God, thank you dear Father for giving me the strength, endurance and courage to stick to this to the end.

”The detailed study of interacting binary systems has revealed the importance of angular momentum in accretion. In many cases, the transferred material cannot land on the accreting star until it has rid itself of most of its angular momentum. This leads to the formation of accretion discs, which turn out to be efficient machines for extracting gravitational potential energy and converting it into radiation.”

Frank, King & Raine
Accretion Power in Astrophysics

Abstract

After the retirement of professor A. Jarrett in 1986, the 1.5-m telescope at Boyden Observatory stood idle for a decade. With the appointment of Dr P. Meintjes, steps were taken to refurbish the telescope with an updated drive control and camera system, which would eventually enable the telescope to be operated as an astrophysical research instrument. After funding became available, upgrading of the drive mechanisms were undertaken by DFM during August and September 2001 and the new SpectraVision $1k \times 1k$ CCD camera, that was on loan from Lawrence Livermore National Laboratory (LLNL), was installed during February 2002. After 16 years, the telescope was ready to be used for gathering data for research projects. The camera was installed with only demonstration software. Software was needed to control the camera and also for data reduction and a photometry pipeline.

During this project, the problems encountered with the baffles, electronics and collimation in the telescope were analyzed and fixed where needed and possible. Manuals were written for the general use of the telescope, as well as the reduction and photometry pipeline. Extinction coefficients for Boyden Observatory were determined.

Software were developed to control the PixelVision CCD camera. A CCD reduction routine that is easy and automatic as far as possible was written and implemented. A photometry pipeline that can be used with vast amounts of data, while producing a high level of accuracy were developed.

The research fields that are making use of the software include gravitational microlens observations, accreting compact objects and Gamma Ray Burst afterglows. A brief overview of these fields are given.

Contents

| | | |
|----------|----------------------------------------------------------------------------------------------|-----------|
| 1 | Boyden Observatory | 1 |
| 1.1 | History | 1 |
| 1.2 | Reviving the UFS-Boyden Observatory | 3 |
| 1.3 | Research aims | 4 |
| 2 | UFS-Boyden Astrophysics program: Scientific motivation for a fully equipped telescope | 5 |
| 2.1 | Microlens follow-up observations | 5 |
| 2.1.1 | Introduction | 5 |
| 2.1.2 | Searching for halo objects | 6 |
| 2.1.3 | The Einstein Ring | 7 |
| 2.1.4 | Magnification | 10 |
| 2.2 | GRB follow-up observations | 13 |
| 2.2.1 | A Theory of Gamma Ray Bursts | 13 |
| 2.2.2 | Gamma-Ray Burst Physics | 15 |
| 2.3 | Accretion driven systems | 16 |
| 2.3.1 | Accretion disc related phenomena | 18 |
| 3 | Upgrade and Instrumentation of UFS-Boyden 1.5-m Telescope | 20 |
| 3.1 | Upgrade | 20 |
| 3.2 | Camera | 22 |
| 3.3 | Filters | 22 |
| 4 | Camera Control and Image Acquisition Software | 23 |
| 4.1 | Observational requirements for system | 23 |
| 4.2 | Software | 23 |
| 4.3 | Camera and Filter Software | 24 |
| 4.3.1 | SPICA | 24 |
| 4.3.2 | Other software | 27 |
| 4.4 | Current status of the telescope | 27 |
| 4.4.1 | Aluminizing of mirrors | 27 |
| 4.4.2 | Electronic noise | 27 |
| 4.4.3 | Electronic and mechanical failures | 28 |
| 4.4.4 | Collimation | 28 |
| 4.4.5 | Baffles | 28 |

| | | |
|----------|-------------------------------------------------------------------|-----------|
| 5 | CCD Images | 34 |
| 5.1 | Origins of Photometry | 34 |
| 5.2 | CCD technology | 35 |
| 5.2.1 | Pixel size and field of view | 36 |
| 5.2.2 | Instrumental Effects in CCD Detectors | 37 |
| 5.3 | Data Reduction | 37 |
| 5.3.1 | Data Reducing Procedure | 40 |
| 5.4 | Photometric Systems | 40 |
| 6 | Photometry using CCD Images | 43 |
| 6.1 | Instrumental Magnitudes | 43 |
| 6.2 | Different Methods of Photometry | 43 |
| 6.2.1 | Differential Photometry | 43 |
| 6.2.2 | Aperture Photometry | 44 |
| 6.2.3 | Photometry from Image Profiles | 44 |
| 6.3 | Sky Brightness | 44 |
| 6.4 | Air Mass | 45 |
| 6.5 | Calibrating Instrumental Magnitudes | 46 |
| 6.5.1 | Calibration without a colour correction | 46 |
| 6.5.2 | Calibration with a colour correction | 47 |
| 6.6 | Atmospheric Extinction Coefficients | 48 |
| 6.6.1 | Second Order Coefficients | 49 |
| 6.6.2 | First Order Coefficients | 50 |
| 6.6.3 | Determining Colour Transformation Coefficients | 52 |
| 6.7 | Standard Stars | 53 |
| 6.7.1 | Choosing Standard stars | 53 |
| 6.8 | Zero points | 54 |
| 6.9 | Determining the night's photometric quality | 55 |
| 6.10 | Accuracies | 57 |
| 7 | A Pipeline for Photometric Measurements | 59 |
| 7.1 | Reduction and Photometry Pipeline | 59 |
| 7.1.1 | CCD reduction | 60 |
| 7.1.2 | Photometry Measurements | 60 |
| 7.1.3 | Determining reduction coefficients | 62 |
| 7.1.4 | Aperture and optimal photometry | 62 |
| 7.1.5 | Colour coefficient determination | 62 |
| 7.2 | Verifying photometric measurement accuracy | 63 |
| 7.2.1 | Scientific publications submitted that used Boyden data | 64 |
| 8 | Conclusion | 69 |
| 8.1 | Image capturing software | 69 |
| 8.2 | Reduction and photometry pipeline | 69 |
| 8.3 | Problems and solutions | 70 |
| 8.4 | Suggestions | 70 |

| | |
|---------------------------------------------------------------------------------------------|-----------|
| A Binary Evolution: Spin-up, spin-down and non-thermal emission from compact objects | 75 |
| A.1 Introduction | 75 |
| A.1.1 Mass transfer vs. mass accretion | 76 |
| A.2 Star-disc interaction: spin-up and spin-down | 77 |
| A.3 Magnetospheric flares | 78 |
| A.4 Observational issues | 79 |
| A.5 Conclusion | 79 |

List of Figures

| | | |
|-----|----------------------------------------------------------------------------------------------------------------------------------------------------------------------------------------------------------------------------------------|----|
| 2.1 | Schematic diagram of microlensing. | 6 |
| 2.2 | A typical microlensing light curve. [6] | 7 |
| 2.3 | Diagram of a typical microlens setup[35]. | 8 |
| 2.4 | Geometry of a perfectly lined-up microlensing system | 10 |
| 2.5 | A typical microlensing lightcurve, showing a modelled microlensing event where the lens is an Earth-sized object, circling a $0.3 M_{\odot}$ star. See text for details. [6] | 13 |
| 2.6 | The Earth as seen from above the south pole, indicating the importance of longitude coverage by Boyden Observatory. | 14 |
| 2.7 | Data illustrating the importance of continual observations. Boyden data are lighter coloured for ease of identification[1]. | 14 |
| 2.8 | A diagram showing the typical contribution of Boyden data in the microlens campaigns. Boyden data in these graphs are marked with f . The data are marked with a "X" for ease of identification[6]. | 14 |
| 3.1 | Quantum efficiency of SiTe chip used in PixelVision camera (UVAR) compared to front illuminated and the standard (Std AR) chips [34]. | 22 |
| 3.2 | Filter transmission curves. <i>Filter data from Kitt Peak Observatory.</i> | 22 |
| 4.1 | Bias frame showing the effects of electronic noise and pixel value counts against count distribution shows clearly the periodic noise present in all the bias frames. This noise is present in all the images as well. | 28 |
| 4.2 | Profiles of flat fields at Boyden taken at twilight and during the observing run on sparse starfield. | 29 |
| 4.3 | Typical profiles of a raw image, a flat field and flat fielded image. | 30 |
| 4.4 | Profiles of a flat fielded image at Boyden flat fielded with the twilight and night sky flat fields respectively. | 31 |
| 4.5 | Hartman screen used for collimation of 1.5-m telescope. | 31 |
| 4.6 | Drawing of the new baffle setup showing the four rings inside the old, shorter baffle. The rings are not to scale. The size of the rings were optically chosen to exclude all of the area visible around the secondary baffle. | 32 |
| 4.7 | Comparable pinhole images of the inside of the telescope tube, showing a very bright, off-axis light source. The image on the left is before the rings are installed, the image on the right after the installation. | 32 |
| 4.8 | Light profiles before and after adding rings to the baffle. The secondary peak is due to a bright off-axis light source placed for evaluating reflection elimination by the rings in the new baffle. | 33 |

| | | |
|-----|------------------------------------------------------------------------------------------------------------------------------------------------------|----|
| 6.1 | Schematic diagram of extinction. | 45 |
| 6.2 | Calculated signal to noise ratio of a bright star (star count=2000) compared to a dim star (star count =200) plotted against the sky count | 58 |
| 7.1 | Schematic outline of the photometry scripts | 59 |
| 7.2 | Fields of E7-97 showing the single star and crowded field M54 with the PSF-star and measured star used for optimal aperture testing shown. | 65 |
| 7.3 | Aperture photometry - Measured instrumental magnitudes for fields in figure 7.2. | 65 |
| 7.4 | Measured instrumental magnitudes for indicated stars in figure 7.2 using optimal photometry. | 66 |
| 7.5 | Fit of catalogue and instrumental magnitudes against atmospheric extinction for Landolt standards 110-229, E6-73, E7-97 and Wolf 629 | 68 |

List of Tables

| | | |
|-----|------------------------------------------------------------------------------------------------------------------------------------------|----|
| 5.1 | Details of common photometric systems.[33] | 42 |
| 7.1 | List of standard stars used for determining the first order, second order and transformation coefficients of the Boyden filters. | 67 |
| 7.2 | Photometric comparison of E7-52 and E7-62 as "unknowns" to evaluate photometry procedures | 67 |

List of Accronyms used

CCD Charge Coupled Device

DUO Disc Unseen Objects

EROS Experience de Recherche d'Objets Sombres

GRB Gamma Ray Bursts

HESS High Energy Stereoscopic System

MACHO MAssive Compact Halo Objects

MOA Microlensing Observations in Astrophysics

MPS Microlensing Planet Search

NRF National Research Foundation

OGLE Optical Gravitational Lensing Experiment

PMT Photo-Multiplier Tube

PLANET Probing Lensing Anomalies NETwork

VHE Very High Energy

UFS University of the Free State

Chapter 1

Boyden Observatory

1.1 History

The history of Boyden Observatory near Bloemfontein is closely linked with the Harvard College Observatory ([24], [5]). Boyden Observatory's history starts in 1879 when Uriah Boyden, a mechanical engineer left \$238 000 to Harvard College to be used for an astronomical observatory at a high enough altitude to overcome the troublesome effects of the atmosphere. The Director of Harvard College Observatory was very keen on building an observatory in the southern hemisphere, allowing access to the Magellanic Clouds. One of the staff members, Prof. Solon Bailey, visited South America to find possible sites with good weather and a clean dry atmospheric region and came up with a hill near Lima in Peru, accordingly named Mount Harvard in 1889. Unfortunately the observation conditions were not good enough and they started searching for a better place in Peru later that season.

One year after Harvard College began making observations from a temporary location at Mount Harvard, it was decided to look for another suitable location, as unstable weather patterns plagued the Mount Harvard site. The decision fell on Arequipa, also in Peru, and this site was made the permanent home of the Observatory. In January 1891 the Director of Harvard College Observatory, Prof. Edward Pickering, came to Arequipa with more equipment, including a 33-cm refractor telescope. Numerous observations were consequently made of Mars, the Moon and the satellites of Jupiter and Saturn. Fortunately Arequipa had a very steady atmosphere, very useful for studying the planets. These succesful observations resulted in the gradual expansion of the infrastructure, and by 1903, the observatory in Arequipa had numerous equipment, some of the most advanced in the world. This equipment included a 61-cm aperture photographic telescope, which was used extensively to produce star atlases containing very faint stars. Although Arequipa proved to be a fairly satisfactory site from the point of view of the results obtained there, the amount of cloud cover was often too much and its distribution inconvenient. South Africa's excellent climatic conditions were fairly well known and in 1908, an expedition under the leadership of Prof. Bailey was sent to South Africa to investigate the possibilities.

This team travelled via Cape Town and Worcester to Hanover in the Western Cape, the first seriously considered sites for the Observatory. Expeditions to Bloemfontein, Kimberley and even Harare were undertaken. Hanover was selected as the primary option with Bloemfontein and

Worcester as secondary options. Observational testing from these sites commenced in 1909 to study atmospheric steadiness and cloud cover. The difference between Bloemfontein and Hanover was very little and although seeing was a bit better at Hanover, Bloemfontein was the more preferable site taking all considerations into account. In 1923 the famous Dr. Harlow Shapley, director of Harvard College Observatory at that time, gave the order for the observatory at Arequipa in Peru to be moved to its new site near Bloemfontein, South Africa - on a koppie 24 km out of the city overlooking Mazelspoort. Observations at Arequipa, Peru, continued until 1926 when they started to dismantle the equipment there in preparation for the great move across the sea. Funds for the transfer came from Harvard and the International Education Board. Dismantling the equipment at Arequipa commenced in 1926 and in February 1927 the instruments were shipped to Bloemfontein. The city authorities were most generous in assisting with the setting up of the observatory by providing a road up the koppie, as well as supplying infrastructure for electricity, water and telephone connections. Observation began in September 1927 and in 1933 the new site was officially completed. At that time the instruments in operation were: the 1.5-m reflector, the 13-inch refractor (33 cm) and the 25-cm Metcalf photographic refractor, all still in operation at Boyden. A 61-cm Bruce Astrograph and 20-cm refractor, as well as some smaller instruments were installed but are not in operation anymore.

When the Observatory at Boyden commenced preliminary operations in 1927, Dr John Stefanos Paraskevopoulos was appointed Director, being the astronomer in charge of Arequipa since 1923. He studied at Athens University, was a corresponding member of the Greek Academy, a Knight of the Order of Phoenix, as well as being a noted astrophysicist. He remained director until 1951, after a long and successful career. The Common mirror in use in the 1.5-m telescope was refigured, but remained a problem as it was only 8.89 cm thick. The observers at that time, Ernest Burton and Michael Bester, who also acted as mechanical technicians, builders and librarians, under the guidance of Paraskevopoulos, devised a manipulation mechanism that deformed the mirror during observations to compensate for the flexure of the mirror. This was probably the first case of adaptive optics being applied to improve image quality.

Until 1968 when Dr Alan H. Jarrett became director, it was agreed that the senior visiting astronomer should take the charge[5]. Many of the astronomers who did research at Boyden were of high international repute and have added enormously to the prestige of the establishment. Some of the famous names include Bok, Velghe, Haffner, Menzel, Lindsey, Wayman, and many other international astronomers who, together with their colleagues, were responsible for several hundreds of publications based on Boyden observations. During its history, the research at Boyden has encompassed many activities. Photographic and photoelectric observations of stars in the Southern Milky Way, the Magellanic clouds and southern hemisphere variable stars contributed much to our understanding of these objects. Boyden is ideally situated for observations of our galactic centre and the Magellanic clouds and became a major centre for such research.¹ A sky patrol program was also operated from the 1950's to the 1970's. Routine surveys were made of transient phenomena such as variable and flare stars and novae. This program was also used to assist with the tracking of the first satellites. Additional research fields included studies on atomic emissions from nebulae, studies of solar flares with a celeostat and photographic and spectroscopic studies of comets.

¹This is also utilized at this point in time with collaborations with the PLANET and Super Macho research groups.

In the 1950's, Harvard University announced it could not continue financing Boyden. The observatory was on the point of closure when astronomers suggested putting Boyden under International sponsorship. The International Boyden Council was then formed, consisting of different astronomical institutions in Europe and North America. For 10 years the consortium operated effectively, but in 1966 the Swedes announced their withdrawal. The vacancy was offered to the University of the Free State. During the 1970's research publications still emanated from Boyden, but it was also the period when the other partners broke off their ties with Boyden - the Council ceased to exist in 1976. The observatory was then offered to the only member of the council close at hand, and the University of the Free State became the owner of this prestigious establishment in April 1976. This marked a turning point in the remarkable history of the observatory - the full facilities of the campus and faculties were now at the disposal of the observatory.

The old Common mirror rocked in its cell. A new mirror cell from the company Heidenreich & Harbeck in Hamburg, was fitted in the early 1960's with a new mirror from Loomis (Custom Optics, Tucson) following in 1968. At that time the worn out drive mechanisms were replaced as well. During the 1980's attempts were made to place the telescope under computer control, and for a while the telescope was controlled by an HP85 microcomputer. This was not very efficient and the telescope became increasingly under-utilized.

1.2 Reviving the UFS-Boyden Observatory

After the retirement of Professor Jarrett in 1986, Boyden Observatory was on the brink of being closed by the University of the Free State. An opportunity to resurrect the Observatory as a fully functional research facility presented itself in 1997 when international research collaborations focusing on microlens planet search projects looked for longitude coverage between the sites in Chile and Australia. The Boyden site is ideally situated to sample the dense star fields towards the galactic center in the microlens follow-up observing campaign. This will be highlighted in chapter 4.

In collaboration with the University of Notre Dame, the newly created astrophysical research group at the UFS approached the NRF for the required funding to invest in the refurbishment of the existing out-dated infrastructure. This resulted in a NRF grant of R 300 000 being allocated to the refurbishment of the 1.5-m telescope, in conjunction with a \$ 46 000 contribution from Prof. D. Bennett, of the Notre Dame University, towards the refurbishment of the telescope. A further \$ 19 000 contribution from the University of Pennsylvania was acquired to help fund the refurbishment.

The requirements of the microlensing follow-up observations demanded very accurate pointing and tracking, as well as photometry of very faint stars. These requirements resulted in the UFS approach the DFM company near Boulder, Colorado, requesting the delivery of a custom made telescope control system. The manufacturing, delivery and installment of the control system amounted to \$ 90 000, and was followed by the delivery of a \$ 50 000 Pixelvision CCD camera, on loan from the Lawrence Livermore National Laboratories (LLNL), in collaboration with Dr. K. Cook, principal investigator of the GRB afterglow follow-up program.

A fruitful international collaboration between the UFS and the international collaborators required quick real-time data transfer between various sites all over the world, hence the need arose to have

internet access on the UFS-Boyden site. Funding was again requested from the NRF for an internet connection between the UFS campus and the UFS-Boyden site, as well as a local-area network on site. This was completed in May 2004, and so after 16 years, the telescope was ready to be used for gathering data for research projects again! The camera was installed with only demonstration software, and it was decided that a project would be needed to write new software to control the camera, which incidentally is the focus of the study.

1.3 Research aims

A brief discussion is presented in chapter 2 that illuminates various aspects surrounding the UFS-Boyden astrophysics research program. In chapter 3 a brief discussion is presented of the refurbishment of the UFS-Boyden telescope for our research program, illuminating the requirements specified by the observational program. Chapter 4 gives a detailed discussion of the camera control and CCD software, specifically aiming at the requirements that had to be met with respect to the main focus of the study, i.e. the development of a CCD photometry pipeline for the research program. Chapters 5 and 6 deal with an overview of relevant CCD characteristics and CCD photometry methods. An outline and verification of the developed reduction pipeline and verification of the photometry methods are presented in chapter 7. The Appendix contains a paper that was published in *African Skies* as part of the research done on accretion systems.

Chapter 2

UFS-Boyden Astrophysics program: Scientific motivation for a fully equipped telescope

In this chapter a brief overview is presented of the various research topics of the UFS astrophysics program. The motivation behind this brief overview is to illuminate the role of the UFS-Boyden 1.5-m telescope in these research initiatives. This brief discussion will focus on the three international collaborations where the UFS-Boyden 1.5-m telescope and personnel is going to play a pivotal role providing observational support, as well as the in-house research programs where UFS personnel are the principle investigators. The program where the UFS-Boyden 1.5-m telescope is utilised for observational support are the microlens planet search, the gamma ray burst afterglow search program and simultaneous multi-wavelength observational campaigns in collaboration with the HESS VHE γ -ray group.

The UFS astrophysics group focuses on accretion related phenomena in galactic accretion driven systems like cataclysmic variables, X-ray binaries and micro-quasars. Various aspects surrounding these programs will be discussed in the following sections, specifically aiming at reviewing the capabilities it will demand from the refurbished telescope and the software that has been developed to support these programs adequately.

2.1 Microlens follow-up observations

2.1.1 Introduction

Einstein's theory of General Relativity gravity is understood as a manifestation of the curvature of spacetime. One consequence of this is that light rays should bend near any mass. In particular, Einstein predicted that the light from a star should bend as it goes past a massive object like the sun. That prediction was first tested and confirmed by Sir Arthur Eddington in 1919 during a total eclipse of the sun. A star that would otherwise not be visible, because it was behind the sun, was observed close to the sun's limb confirming the bending of light by gravity. These observations showed that stellar positions close to the rim of the blocked-out Sun shifted on average by an

amount of $\Delta\phi \sim 1.73''$, consistent with the predictions of the newly developed theory of General Relativity.

In 1937 Zwicky [45] noted that the bending of light by massive objects should lead to gravitational lensing: the focusing of light from a distant object by a mass that lies in the line-of-sight between the distant object and the observer. At the time the prediction was nothing more than an interesting curiosity because the technical means to test it simply did not exist, and would not exist for another sixty years! Today, gravitational lensing not only provides a beautiful test of Einstein's theory, but also provides a tool for investigating the halo of dark matter thought to surround the Milky Way, i.e. the so called massive compact halo objects (MACHO's) which may play a dominant role in the dynamics of stars in the spiral arms.

The basic idea, as pointed out by Bodhan Paczyński in 1986 ([32]), is that if the galactic halo contains these dark objects, with masses between that of Jupiter (about $1/1000 M_\odot$) and very dim stars (e.g. brown dwarfs) with masses too small (less than $1/10 M_\odot$) to trigger thermonuclear ignition, then once in a while these massive halo objects should cross the line-of-sight between the Earth and a more distant luminous star. If the halo object gets close enough to the line-of-sight we should see a noticeable lensing effect, characterised by a temporary brightening of the light from the distant star. This effect is called microlensing.

2.1.2 Searching for halo objects

Several international teams, PLANET, MOA, EROS, MACHO, OGLE and DUO are searching for halo objects and planets using the stars in the bulge of our own Milky Way and the Large Magellanic Cloud (LMC), as the back-drop against which these unseen objects move. The basic idea is illustrated in figure 2.1.

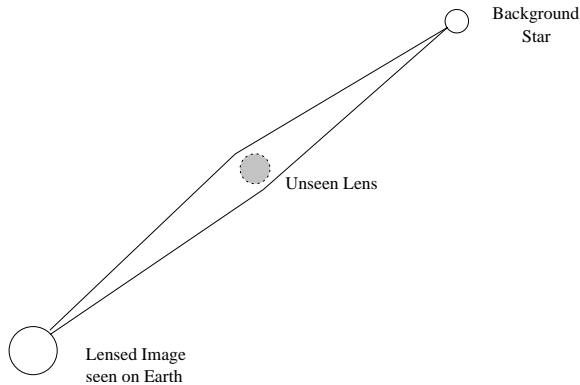


Figure 2.1: Schematic diagram of microlensing.

Light from a star is deflected and indeed focused, by a passing halo object, the unseen lens. This object acts as a gravitational lens. In principle, by measuring the distribution and rate of microlensing events we could learn something about the nature and distribution of these halo objects. In practice, this is very difficult because these accidental line-ups occur infrequently. Typically the microlensing rate is only $\sim 7.3 \times 10^{-7}$ events per star per year [6]. This is a rate of 1 to 2 events in 10 million! This illustrates that the detection of an event presents an enormous observational challenge. The EROS, MACHO and OGLE teams monitor about 4 million stars simultaneously.

The light curve of a microlensing event is precisely predicted by general relativity. Also, microlensing events are singular events: a star appears to brighten then dim, and this sequence is not repeated. Another interesting signature of microlensing is that the effect is achromatic to first order: that is, it does not depend on the colour of the light if the source and lens are compact. Therefore, observation of a star through two filters, usually blue and red, reveals identical light curves. No currently known stellar phenomena, other than microlensing, would produce such a behaviour. A typical light curves is shown in fig.2.2.

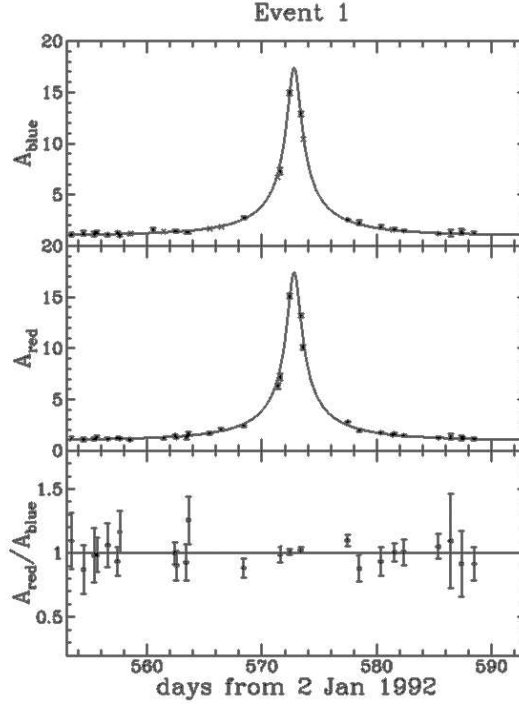


Figure 2.2: A typical microlensing light curve. [6]

Notice the perfectly symmetrical nature of the light curves and the fact that the red and blue light curves are indeed the same. This is very convincing evidence that this is, in fact, the light curve of a microlensing event.

2.1.3 The Einstein Ring

Suppose the Earth, a halo object and a star, are almost lined up (fig. 2.3). In the absence of gravitational lensing the light from the star would travel from the star directly along the line-of-sight to the Earth. The presence of the halo object however, causes light from the star, which would otherwise have missed the Earth, to bend towards the Earth. The light now appears to come from the direction of the image of the star, i.e. the apparent position. There is another image on the other side of the halo object due to symmetry.

The distance between the Earth and the background (source) star is denoted by L — this would be 55kpc for a star in the LMC. The distance between the Earth and the halo object is R . The distance between the image and the halo object is d . The angle between the halo object and the

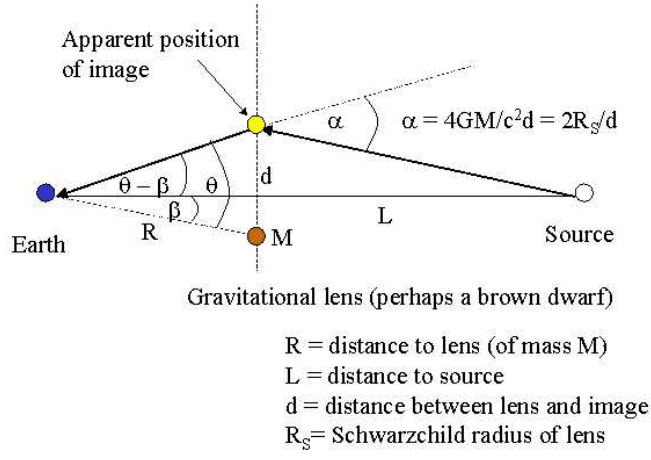


Figure 2.3: Diagram of a typical microlens setup[35].

apparent position of the star is denoted by β , while the angle between the halo object and the star's image is denoted by θ . Obviously, the angle between the star and its image is $\theta - \beta$. The light from the star bends by an angle α , which according to general relativity [26] is given by

$$\alpha = \frac{4GM}{c^2 d}. \quad (2.1)$$

The formula can be written in terms of the Schwarzschild radius, $R_s = 2GM/c^2$:

$$\alpha = \frac{2R_s}{d}. \quad (2.2)$$

For simplicity, we shall assume that the star is very much further away from Earth than the halo object; that is, we shall assume that $L \gg R$. With this assumption we may write the approximate equation $\alpha = \theta - \beta$ [35]. When we combine it with 2.2 we get

$$\theta - \beta = 2\frac{R_s}{d}. \quad (2.3)$$

For small angles

$$d = R\theta, \quad (2.4)$$

which, when combined with 2.3 gives

$$\theta - \beta = 2\frac{R_s}{R\theta}. \quad (2.5)$$

A re-arrangement of 2.5 leads to the quadratic equation

$$\theta^2 - \beta\theta - 2\frac{R_s}{R} = 0, \quad (2.6)$$

whose solutions q_1 and q_2 are

$$\theta_1 = \frac{\beta}{2} + \left(\frac{\beta^2}{4} + 2\frac{R_s}{R} \right)^{1/2}, \quad (2.7)$$

$$\theta_2 = \frac{\beta}{2} - \left(\frac{\beta^2}{4} + 2 \frac{R_S}{R} \right)^{1/2}. \quad (2.8)$$

The θ_1 solution is slightly larger than the angle β , the angular separation between the star and the halo object. This solution corresponds to an image that is displaced away from the line-of-sight. The θ_2 solution corresponds to a second image displaced away from the halo object. In fig.2.3 the second image would lie below the gravitational lens.

When the star and halo object is perfectly aligned, the angle β between the star and the halo object is zero. In that case, we find from 2.7 and 2.8

$$\theta_1(\beta = 0) = + \left(2 \frac{R_S}{R} \right)^{1/2}, \quad (2.9)$$

$$\theta_2(\beta = 0) = - \left(2 \frac{R_S}{R} \right)^{1/2}. \quad (2.10)$$

The images are of course displaced symmetrically about the lens. In fact, because of the rotational symmetry about the line-of-sight there would, in fact, be a ring of images about the halo object. The halo object would have a ring called an Einstein Ring (R_E). The radius of the ring R_E , at the position of the halo object, is given by

$$R_E = R\theta_1(\beta = 0) = (2R_S R)^{1/2}. \quad (2.11)$$

The radius R_E is called the Einstein Radius. Alternatively, the Einstein radius can be written as [2].

$$R_E = \left(\frac{4GM Dx(1-x)}{c^2} \right)^{1/2} \quad (2.12)$$

or as

$$R_E = 2.5 \left(\frac{M}{M_\odot} \frac{Dx(1-x)}{1\text{kpc}} \right)^{1/2} \text{AU} \quad (2.13)$$

where M is the lens mass, D the observer–star distance and Dx the observer–lens distance. From this is evident that the Einstein–radius gives a way to determine the mass of the unseen lens. As an example, consider the Einstein radius for a halo object that is 10 kpc away, and which has a Schwarzschild radius of $R_S = 1/10$ km, i.e. an object with 1/30th the mass of the sun. The Einstein radius will be

$$R_E = (2 \times 10^{-1} \times 3.1 \times 10^{17})^{\frac{1}{2}} = 249 \times 10^6 \text{ km}.$$

This is about 1.7 AU ; therefore, the ring would be slightly larger than the orbit of Mars. The diameter of the ring in arcseconds is:

$$\begin{aligned} \text{Angular diameter} &= \frac{2R_E}{R} \frac{360}{2\pi} 3600'' \\ &= 2 \times \frac{2.49 \times 10^8}{3.1 \times 10^{17}} \frac{360}{2\pi} 3600 \\ &= 3.3 \times 10^{-4}'' . \end{aligned}$$

The Einstein radius will thus be about 1/10 of a milliarcsecond. At present, such a tiny angle is utterly beyond our ability to resolve. This confirms why this process is being referred to as microlensing. However, from an observing point of view, the magnification of the background star, depending on the intrinsic properties of the lensing object, is of more importance, and will be discussed in the following section.

2.1.4 Magnification

In the above discussion the gravitational lens is considered at a fixed angular separation β from a star. In reality, the angular separation would always be changing because of the relative motion of the lens and the star. This causes the total brightness of the two images to change in a very special way. The amount of light received from a star is determined by the solid angle subtended by the star. The solid angle is just the apparent angular area of the star in the sky. The lensing effect increases the solid angle over which we receive light, thereby increasing the amount of light we receive. So if we can calculate the solid angle of the star in the absence of lensing and the solid angle with lensing the light magnification would be simply

$$m = \frac{\text{total solid angle with lensing}}{\text{solid angle without lensing}}.$$

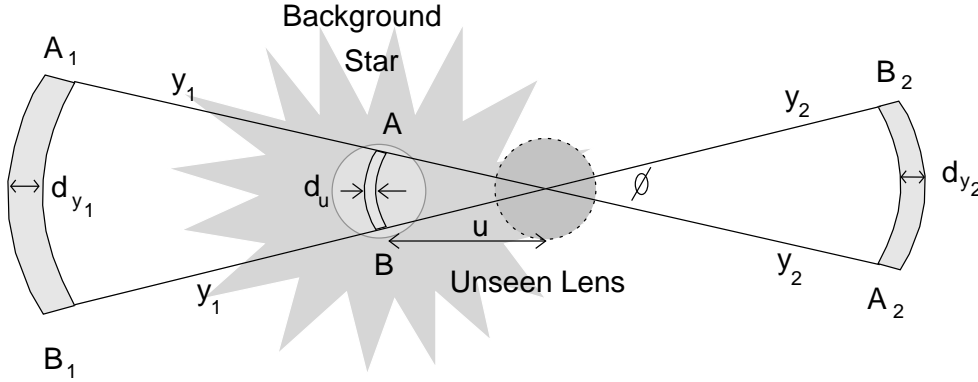


Figure 2.4: Geometry of a perfectly lined-up microlensing system

In figure 2.4, the respective positions of the lens and the background star is shown, as is observed from Earth at a specific β . Consider a strip of width d_u on the star's surface. Let u be the distance between the lens and the points A and B on the strip. Light from these points travels out in all directions; however, the only rays that we need consider are the ones that travel to points A_1 , B_1 , A_2 and B_2 . In the absence of lensing the light from the points A and B would come straight towards us. But because of lensing the light from point A appears to come from the points A_1 and A_2 ; the light from point B appears to come from the points B_1 and B_2 . The lensing effect therefore creates two image strips of width d_{y1} and d_{y2} , to the left and right of the lens, is illustrated in figure 2.4. Let the radial distance from the lens to the points A_1 and B_1 be y_1 and let y_2 be the radial distance from the lens to the points A_2 and B_2 .

The amount of light E from each strip is just the flux f (the energy per unit area per second) times the area of the strip:

$$E = f \times \text{Area} = f u \phi d_u \quad (2.14)$$

$$E_1 = f \times \text{Area} = f y_1 \phi d_{y_1} \quad (2.15)$$

$$E_2 = f \times \text{Area} = f y_2 \phi d_{y_2}, \quad (2.16)$$

where ϕ is the angle between the points A and B , relative to the lens. (We have used the fact that the length of an arc = its radius times its angular size.) Therefore, the magnification m is just

$$m = \frac{E_1 + E_2}{E} = \frac{y_1}{u} \frac{d_{y_1}}{d_u} + \frac{y_2}{u} \frac{d_{y_2}}{d_u}. \quad (2.17)$$

Now follows that

$$u = R\beta, y_1 = R\theta_1, y_2 = R\theta_2. \quad (2.18)$$

and

$$\begin{aligned} \frac{d_{y_1}}{d_u} &= \frac{1}{2} \left(1 + \frac{\beta}{(\beta^2 + 8R_S/R)^{1/2}} \right) \\ &= \frac{1}{2} \left(1 + \frac{u}{(u^2 + 4R_E^2)^{1/2}} \right) \end{aligned} \quad (2.19)$$

$$\begin{aligned} \frac{d_{y_2}}{d_u} &= \frac{1}{2} \left(\beta(\beta^2 + 8R_S/R)^{1/2} - 1 \right) \\ &= \frac{1}{2} \left(\frac{u}{(u^2 + 4R_E^2)^{1/2}} - 1 \right). \end{aligned} \quad (2.20)$$

From 2.18 and 2.7 and 2.8 we can write

$$\begin{aligned} y_1 = R\theta_1 &= R \frac{\beta}{2} + R \left(\frac{\beta^2}{4} + 2 \frac{R_S}{R} \right)^{1/2} \\ &= \frac{1}{2} \left(u + (u^2 + 4R_E^2)^{1/2} \right) \end{aligned} \quad (2.21)$$

$$\begin{aligned} y_2 = R\theta_2 &= R \left(\frac{\beta^2}{4} + 2 \frac{R_S}{R} \right)^{1/2} - \frac{R\beta}{2} \\ &= \frac{1}{2} ((u^2 + 4R_E^2)^{1/2} - u). \end{aligned} \quad (2.22)$$

Substitute 2.19, 2.20, 2.21 and 2.22 into 2.17, and the magnification m as a function of the distance u of the lens from the line-of-sight to the star becomes:

$$m = \frac{u^2 + 2R_E^2}{u(u^2 + 4R_E^2)^{1/2}}. \quad (2.23)$$

This can be further simplified by writing u in units of the Einstein radius R_E . Divide u by the Einstein radius in 2.23. This gives the formula

$$m = \frac{u^2 + 2}{u(u^2 + 4)^{1/2}}. \quad (2.24)$$

This means that if a star is at $3R_E$, the magnification is 1.017, at $1R_E$ 1.34 and at $\frac{1}{2}R_E$ 4.366. As the lens moves across the sky, the distance u will change; it will be a function $u(t)$ of the time t . Assume that the lens moves in a straight line across the sky at a constant speed V . The distance

travelled in time t is then $D = Vt$. At some time, $t = 0$, the star and lens will be closest together: $u_0 = u(t = 0)$. This distance is at right-angles to the direction of motion of the lens. At any other time t , the distance $u(t)$ will be the hypotenuse of a right-angled triangle; the other side is u_0 and the third is Vt/R_E . Divide Vt by R_E because we are measuring lengths in units of the Einstein radius. From Pythagoras' theorem we have for any other time t

$$u(t) = \left(u_0^2 + \frac{V^2}{R_E^2} t^2 \right)^{1/2}. \quad (2.25)$$

The time to cross a distance equal to one Einstein radius is called the lensing time (D_t). The lensing time can conveniently be written as [2].

$$D_t = R_E/V \approx 65 \left(\frac{M}{M_\odot} \right)^{1/2} \text{ days.}$$

Symmetry dictates that the magnification will happen with one Einstein-radius on both sides of the lens. The magnification crossing time will thus be given by $130(M/M_\odot)^{1/2}$. Depending thus on the mass of the lens, the lensing time can be anywhere from hours to weeks, e.g. for a $1 M_\oplus$ object, $M_\odot / M_\oplus = 332946$, and it will thus have a lensing time of

$$D_t = 130 \times \sqrt{\frac{1}{332946}} = 0.225 \text{ days} = 5.4 \text{ hours,}$$

or for a Jupiter mass planet, with $M_{Jupiter}/M_\oplus = 318$, we have

$$D_t = 130 \times \sqrt{\frac{318}{332946}} = 4.017 \text{ days.}$$

Usually, $u(t)$ is written in terms of the lensing time:

$$u(t) = \left(u_0^2 + \frac{t^2}{D_t^2} \right)^{1/2}. \quad (2.26)$$

The formula's given by 2.24 and 2.26 provide a precise description of the microlensing light curve.

A significant number of planets with masses down to $1 M_\oplus$ can be detected via gravitational microlensing if microlensing events toward the Galactic bulge are monitored approximately hourly with photometric precision of $0.5 - 1.0\%$, which is readily achievable in crowded stellar images. The results of probability calculations determine the optimal planetary search strategy [6]. From the examples above it is clear that if the capacity of the follow-up system is saturated, it is best to concentrate follow-up observations on events with $m \approx 1.34$. This effect is basically geometric: planets that are outside the lensing zone tend to give rise to isolated events that are not associated with a stellar lensing event detected by the survey system. It is optimal thus to search for planets within the lensing zone. It is suggested that it will be easier to detect Earth-mass planets by monitoring lensing events in smaller stars, than giant star events [6]. It may be possible though to detect Earth-size planets using a combination of infrared and optical observations [21]. Bennett and Rhie [6] have shown that planets with masses as small as $1 M_\oplus$ can be detected via gravitational microlensing.

A typical light curve that can be expected from an Earth-size planet detection is shown in figure 2.5. Here the microlensing light curves are plotted for mass ratios M/M_{\odot} of 10^{-4} ($1 M_{\oplus}$) and 10^{-5} ($10 M_{\oplus}$) and separations, in terms of the Einstein-radius, $l = 0.8$ and $l = 1.3$. The main plots are for a stellar radius of $R_s = R_{star}/R_E = 0.003$ while the insets show light curves for radii of 0.006, 0.013 and 0.03 as well. The amplitude of the maximum light curve deviation decreases with increasing R_s . The dashed curves represents the unperturbed single lens light curves.

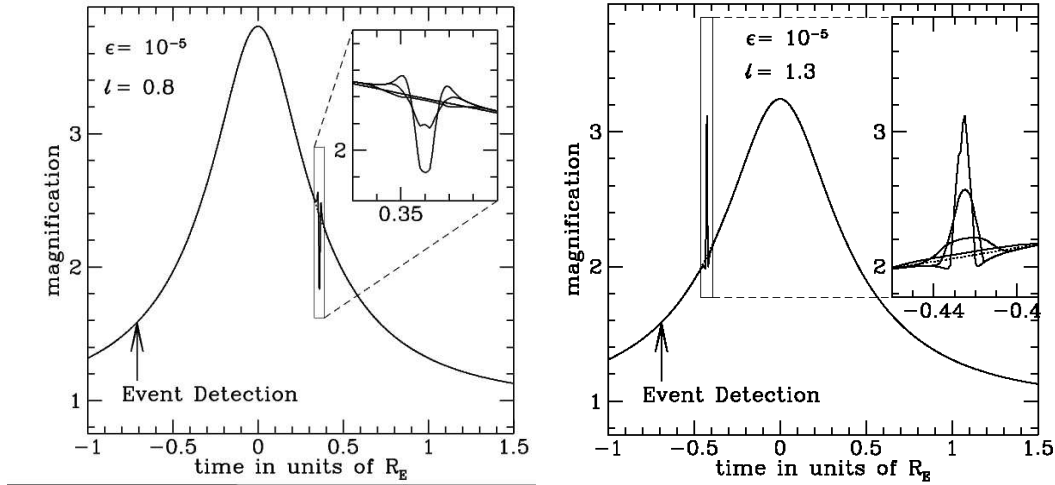


Figure 2.5: A typical microlensing lightcurve, showing a modelled microlensing event where the lens is an Earth-sized object, circling a $0.3 M_{\odot}$ star. See text for details. [6]

The lensing time for Earth-mass planets suggest that continuous coverage of the system undergoing lensing is needed, as observations less than two hours apart result in a successful observing of a planet. The longitudinal location of Boyden is of extreme importance in the continuous observing of microlensing candidates, as can be seen in figure 2.6. The significance of Boyden observations were adequately illustrated with the observations of the 2002 MOA BLG 33 object, as Boyden data supplied the observational support to model the critical Einstein lens effects (fig.2.7). Numerous events were followed during the 2002–2003 MACHO campaign and the 2004 PLANET campaign (fig.2.8).

2.2 GRB follow-up observations

2.2.1 A Theory of Gamma Ray Bursts

Until 1995 the literature on gamma ray bursts (GRB's) contained over 100 different theories on the causes of these energetic events [29]. With the discovery of optical afterglows and subsequent distance determinations, there remain basically two possible explanations:

The exploding star scenario These models predict that the GRB's are the end-states of short-lived massive stars with low space velocities. A consequence is that GRB's should be mainly found in or near star forming regions where these type of stars could form. Examples of this kind of models are the "failed supernova" model of Woosley[42], and the "hypernova" model of Paczyński [32].

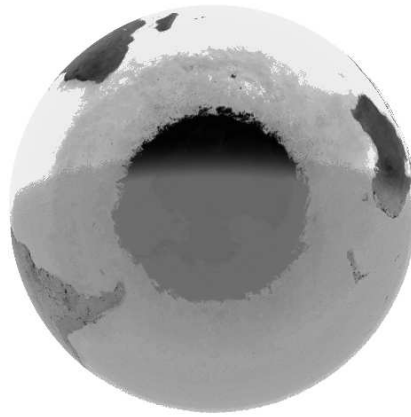


Figure 2.6: The Earth as seen from above the south pole, indicating the importance of longitude coverage by Boyden Observatory.

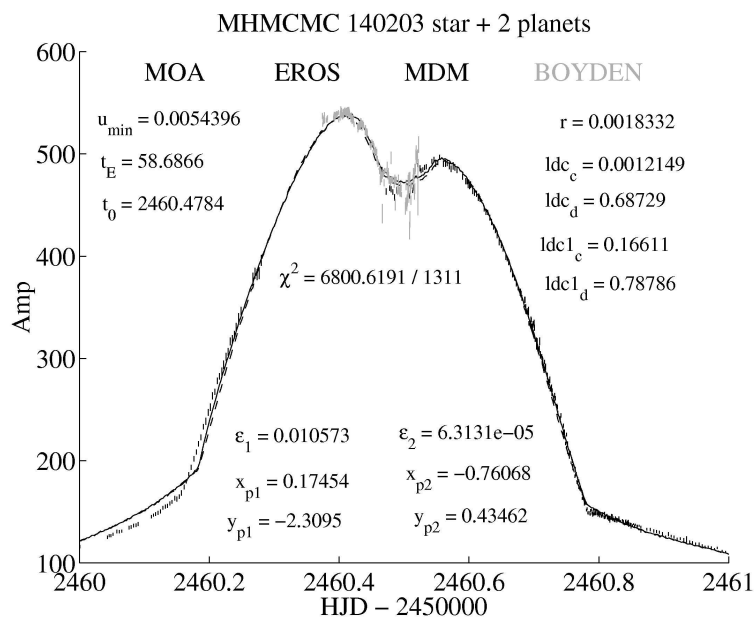


Figure 2.7: Data illustrating the importance of continual observations. Boyden data are lighter coloured for ease of identification[1].

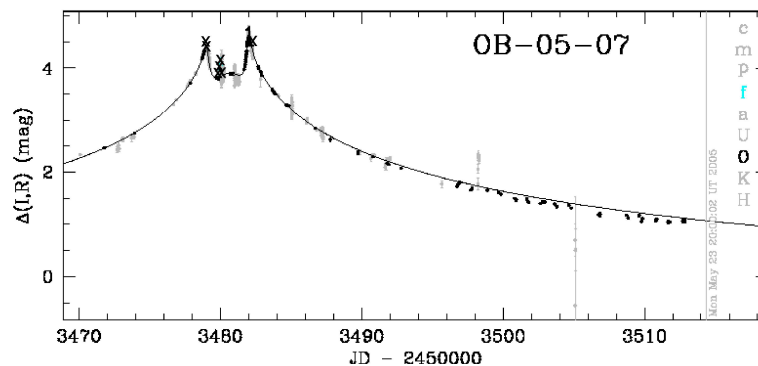


Figure 2.8: A diagram showing the typical contribution of Boyden data in the microlens campaigns. Boyden data in these graphs are marked with f. The data are marked with a "X" for ease of identification[6].

A compact binary merger This could be either a binary neutron star [31] or a merger of a black hole and a neutron star [32]. In either case the system should have experienced and survived two supernova explosions. The GRB progenitor could therefore have high space velocity and could have moved a significant distance from where it was formed.

2.2.2 Gamma-Ray Burst Physics

Gamma-ray bursts (GRB) are sudden, intense flashes of gamma-rays which, for a few blinding seconds, light up in an otherwise fairly dark gamma-ray sky. They are detected at the rate of about one a day, and during outburst, they outshine every other gamma-ray source in the sky, including the sun[29]. Major advances have been made in the last three or four years, including the discovery of slowly fading x-ray, optical and radio afterglows of GRBs, the identification of host galaxies at cosmological distances, and finding evidence for many of them being associated with star forming regions and possibly supernovae. Progress has been made in understanding how the GRB and afterglow radiation arises in terms of a relativistic fireball shock model.

Until a few years ago, GRB were thought to be just that, bursts of gamma-rays which were largely devoid of any observable traces at any other wavelengths. GRBs were first reported in 1973, based on 1969-71 observations by the Vela military satellites monitoring for nuclear explosions in verification of the Nuclear Test Ban Treaty. When these mysterious gamma-ray flashes were first detected, which did not come from Earth's direction, the first suspicion (quickly abandoned) was that they might be the product of an advanced extraterrestrial civilization. Soon, however, it was realized that this was a new and extremely puzzling cosmic phenomenon. A major advance occurred in 1991 with the launch of the Compton Gamma-Ray Observatory (CGRO). The all-sky survey from the Burst and Transient Experiment (BATSE) onboard CGRO, which measured about 3000 bursts, showed that they were isotropically distributed, suggesting a cosmological distribution, with no dipole and quadrupole components. This isotropic distribution and the brightness distribution provided strong support for a cosmological origin, and the detailed gamma-ray spectra and time histories imposed significant constraints on viable models, which led to the development of the fireball shock model.

A dramatic development in the last several years has been the measurement and localisation of fading x-ray signals in a number of GRB observations by the Beppo-SAX satellite . These afterglows, lasting typically for weeks, made possible the optical and radio detection of afterglows, which, as fading beacons, mark the location of the fiery and brief GRB event. These afterglows in turn enabled the measurement of redshift distances, the identification of host galaxies, and the confirmation that GRB were, as suspected, at cosmological distances of the order of billions of light-years, similar to those of the most distant galaxies and quasars. Even at those distances they appear so bright that their energy output during its brief peak period has to be larger than that of any other type of source, of the order of a solar rest-mass if isotropic, or some percent of that if collimated[32]. This energy output rate is comparable to burning up the entire mass-energy of the sun in a few tens of seconds, or to emit over that same period of time as much energy as our entire Milky Way does in a hundred years.

The energy density in a GRB event is so large that an optically thick pair/photon fireball is ex-

pected to form, which will expand carrying with itself some fraction of baryons. To explain the observations, the relativistic fireball shock model was proposed by Rees and Meszaros [36]. This model has been quite successful in explaining the various features of GRB's. The successful prediction of the general X-ray and optical behaviour of GRB 970228 afterglow by Rees and Mészáros [30] sparked interest in the afterglows of GRB's. Since then more and more afterglows have been studied in detail, and a number of interesting developments have occurred. A prompt optical flash (also predicted by theory) was found in one burst; many afterglows were found to be collimated. A new variety of softer bursts dubbed "X-ray flashes" have been identified, which are very similar to classical GRB but having a softer spectrum. Many of the afterglows identified by Beppo-SAX (all belonging to the class of "long" bursts, >10 s duration) have been shown to be associated with massive young stars, and in some cases a peculiar supernova ("hypernova") may be associated, as suggested by Woosley[42] and Paczynski[32]. Other work has concentrated on modeling the central engine responsible for the energy release. The main ideas are the formation of a several solar mass black hole with a torus of debris around it which is rapidly accreted, and which feeds an MHD or electron-positron-baryon jet. This can result from either the merger of a compact binary, such as a double neutron star (which is expected to lead to short bursts (< 10 s), observed in gamma-rays but so far without identified long-wavelength afterglows) or by the collapse of the fast-rotating core of a massive star, in some cases dubbed a collapsar, which leads to long bursts (>10 s) and could be associated with a supernova-like phenomenon.

2.3 Accretion driven systems

The UFS astrophysics group is intensely involved in the study of accretion related phenomena in close binary stars, as well as X-ray binaries and the so-called microquasars. Close binary stars are stars locked in orbit around one another, both orbiting the systems common center of mass (CM) with an orbital period (P_{orb}) of a few hours. In most cases the system consists of an ordinary main sequence red dwarf (i.e. the secondary) and a white dwarf (i.e. the primary). The short binary period implies that these systems are extremely compact, having a binary separation

$$a \sim 10^{10} \left(\frac{P}{hr} \right)^{2/3} \text{ cm}$$

implying that the whole system can easily fit inside the sun.

The X-ray binaries and the so-called microquasars, on the other hand, are binary systems where the secondary star is usually an O-type or B-type main sequence star, with the primary a more exotic compact object, usually a neutron star or a black hole. These systems are more massive than the close binaries and can have orbital periods of a few days or weeks.

From an observational point of view, these sources display fascinating transient phenomena, all of which are intimately linked to the accretion of mass by the compact object. The mode of mass accretion on the other hand is intimately linked to the mass transfer process, the binary separation, which in turn determines the orbital period, as well as the magnetic properties of the primary star. A qualitative discussion focussing only on the most relevant aspects relating to mass transfer and accretion will be presented.

In these binaries the secondary star is the most cases filling its critical Roche surface, allowing the outer envelope of the star to be in contact with the region of zero effective gravity, i.e. the L_1 Lagrangian point [20]. Thermal motions result in gas from the secondary star's envelope to stream across the L_1 point, resulting in mass transfer from the secondary to the primary. As a result of the rotation of the binary, the material leaving L_1 will have an enormous amount of specific angular momentum. For illustration purposes, the specific angular momentum of material orbiting the CM at L_1 is given by

$$j_{L_1} \sim V_\phi L_1 R_{L_1}.$$

Here $R_{L_1} = f(q)a$, where

$$f(q) = 0.5 - 0.277 \log q ; \quad q = \frac{M_2}{M_1}$$

and a representing the binary separation [20]

$$\text{X-ray binary (XRB)} \quad a \approx 2 \times 10^{12} \left(\frac{M_1}{M_\odot} \right)^{1/3} \left(\frac{P_{orb}}{\text{week}} \right)^{2/3} \text{ cm} \quad (2.27)$$

$$\text{Close binary (CB)} \quad a \approx 3 \times 10^{10} \left(\frac{M_1}{M_\odot} \right)^{1/3} \left(\frac{P_{orb}}{\text{hours}} \right)^{2/3} \text{ cm} \quad (2.28)$$

The orbital velocity of the gas at the inner Lagrangian point L_1 is

$$\begin{aligned} V_{\phi, L_1} &\approx a_2 \Omega_{orb} \\ &\approx \left(\frac{M_1}{M_1 + M_2} \right) a \Omega_{orb}. \end{aligned}$$

For $M_1 \sim 1 M_\odot$ and $q \sim 1$, we get

$$\text{XRB} \quad V_{\phi, L_1} \approx 50 \text{ km/s} \left(\frac{a}{10^{12} \text{ cm}} \right) \left(\frac{P}{\text{week}} \right)^{-1} \quad (2.29)$$

$$\text{CB} \quad V_{\phi, L_1} \approx 260 \text{ km/s} \left(\frac{a}{3 \times 10^{10} \text{ cm}} \right) \left(\frac{P}{\text{hours}} \right)^{-1} \quad (2.30)$$

resulting in the material leaving the L_1 region having specific angular momentum of

$$\text{XRB} \quad j_{L_1} \sim 2.5 \times 10^{18} \left(\frac{V_{\phi, L_1}}{30 \text{ km/s}} \right) \left(\frac{R_{L_1}}{5 \times 10^{11} \text{ cm}} \right) \text{ cm}^2 \text{ s}^{-1} \quad (2.31)$$

$$\text{CB} \quad j_{L_1} \sim 4 \times 10^{17} \left(\frac{V_{\phi, L_1}}{260 \text{ km/s}} \right) \left(\frac{R_{L_1}}{7 \times 10^{10} \text{ cm}} \right) \text{ cm}^2 \text{ s}^{-1} \quad (2.32)$$

Before the material can eventually accrete onto the compact object it has to rid itself from this initial angular momentum load.

The standard mode of accretion, if the binary is wide enough, is through an accretion disc, unless the binary is compact enough, allowing the ballistic stream to interact directly with the magnetic field of the compact object, from where it is channelled to the surface where it can accrete and

liberate gravitational potential energy as heat and radiation. The last mode of accretion occurs mainly in the so-called AM-Her type stars, a sub-class of the magnetic cataclysmic variables. The most fascinating mode of accretion from an observational point of view, is through an accretion disc. In this mode of accretion, disc viscosity facilitates the accretion rate onto the compact object.

2.3.1 Accretion disc related phenomena

The observable properties of accretion discs surrounding compact accreting objects provide an unique opportunity to study important transport related phenomena, e.g. momentum and radiation. The transport of angular momentum in an accretion disc is intimately tied to the rate of mass accretion and hence the resultant conversion of gravitational potential energy of the accreted material to heat and observable radiation. In general this is given by

$$L_{acc} \approx \frac{GM_1 \dot{M}_1}{R_{*,1}} \quad (2.33)$$

and for a white dwarf and neutron star respectively we have

$$L_{acc,WD} \sim 10^{34} \text{erg s}^{-1} \left(\frac{M_1}{M_\odot} \right) \left(\frac{\dot{M}_1}{10^{17} \text{g s}^{-1}} \right) \left(\frac{R}{10^9 \text{cm}} \right)^{-1} \quad (2.34)$$

$$L_{acc,NS} \sim 10^{37} \text{erg s}^{-1} \left(\frac{M_1}{M_\odot} \right) \left(\frac{\dot{M}_1}{10^{17} \text{g s}^{-1}} \right) \left(\frac{R}{10^6 \text{cm}} \right)^{-1} \quad (2.35)$$

The mechanism facilitating this mass inflow and resultant accretion is the so-called disc viscosity, the nature of which is still uncertain and a topic of intense study.

The angular momentum dissipation of disc material, allowing inflow and resultant accretion, is facilitated through the disc stresses as a result of the differential nature characteristic of Keplerian motion, i.e.

$$\Omega \sim R^{-3/2}.$$

This velocity gradient allows momentum exchange between layers orbiting with different velocities. This is the physical basis of viscosity, resulting in disc stresses being generated as a result of the differential motion. As a result of the viscosity in the disc the fluid loses mechanical energy, which is being converted to heat. The heat generation rate per unit volume is

$$\frac{\partial q}{\partial t} = -\pi_{ij} \frac{\partial v_i}{\partial x_j} \quad (2.36)$$

where

$$\pi_{ij} = -2\mu \left[\frac{1}{2} \left(\frac{\partial v_i}{\partial x_j} + \frac{\partial v_j}{\partial x_i} \right) - \frac{1}{3} \delta_{ij} \nabla \cdot \vec{v} \right]$$

represents the so-called stress tensor. Prominent in this equation is the value of the coefficient of viscosity (μ) and the velocity shear

$$\Lambda_{ij} = \frac{1}{2} \left(\frac{\partial v_i}{\partial x_j} + \frac{\partial v_j}{\partial x_i} \right).$$

For an incompressible fluid ($\nabla \cdot \vec{v} = 0$) the heat generation rate per unit volume is

$$\frac{dq}{dt} = \frac{1}{2}\mu \left(\frac{\partial v_i}{\partial x_j} + \frac{\partial v_j}{\partial x_i} \right)^2; \quad (2.37)$$

which in a cylindrical coordinate system reduces to

$$\frac{dq}{dt} = \frac{1}{2}\mu \left(\frac{\partial v_\phi}{\partial R} \right)^2 \text{ erg cm}^{-3} \text{ s}^{-1} \quad (2.38)$$

in terms of the dominant contribution, coming from the differential Keplerian motion. The structure of the accretion discs around compact objects has been well explained in terms of the so-called α -disc model [20]. The parameter of least certainty is the disc viscosity μ , which determines the disc brightness which can be constrained by UBVRI photometry and spectra-photometry. This provides good observational data of disc brightness profiles which can allow the constraining of μ , which can be fed back into disc models evaluating mass inflow and mass accretion in those systems. This can be weighted with observational data of accretion induced luminosity using UV and X-ray satellite data.

The discussions in the previous sections aimed at providing an overview of the research being carried out by the UFS astrophysics group. The discussions which are to follow will focus on the main theme of this study, namely the refurbishment of the UFS-Boyden telescope and the data analysis software that has been developed to facilitate the observational aspects of the program.

Chapter 3

Upgrade and Instrumentation of UFS-Boyden 1.5-m Telescope

3.1 Upgrade

It was mentioned earlier that the 1.5-m UFS-Boyden Cassegrain telescope was upgraded with funds from the Universities of Notre-Dame, Pennsylvania and the Free State(NRF grant). The upgrade consisted of the replacement of the drive motors, installation of encoders on both axes of the telescope and the dome, and the adjustment and calibration of the focus motors. The optical alignment of the primary and secondary mirrors was adjusted during the initial upgrade and again more recently.

DFM Engineering was contracted to install a telescope control system and to provide engineering and technical services needed to get the telescope functioning in a research manner. Based upon a previous visit by Dr. Frank Melsheimer, new secondary drives were designed and fabricated in the DFM Engineering shops for the Right Ascension and Declination motions and for the focus drive. A quality focus position encoder was also added to allow precise and repeatable focusing of the telescope. The declination drive installation was a bit problematic. A cutout was needed in the declination counterweight that houses the declination worm gear set to allow access for the new secondary gearing. This cutout required three days of drilling a series of holes then sawing through the remaining metal. The sides of the new cutout were then carefully cleaned with a grinder and files. The declination drive worm and wheel were cleaned and re-lubricated with a special grease that does not thicken at low temperatures. Lubrication tubes were provided to allow lubricating the declination worm and wheel from outside of the housing.

The existing single speed focus motor was replaced with a D.C. servo motor. The new motor provides two speed operation from the hand paddle and a focus setting position capability from the control system. This allows two speeds, one for fast movement, and another slower speed for fine control. An absolute encoder was added to provide focus position with a resolution of 12 microns at the secondary mirror. One resolution element produces a change in the image diameter due to focus of less than 0.1 arc seconds. Ageing resulted in wearing of the secondary mirror's attachment which had to be fixed. A series of holes were drilled into the casing, secured with split-pins to

limit the backlash motion of the secondary mirror. This was complemented by a realignment of the primary mirror since the backlash of the secondary affected the collimation and preventing satisfactory declination position repeatability.

The dome was encoded to provide azimuth information for the automatic dome control feature of the control system. The control system was interfaced to the existing dome motors so the dome may be controlled from the hand paddle or automatically via the control interface. In the process of installing the dome encoder and controls, recommendations were made for the maintenance of the dome drive gear reducers - these gear reducers have been in service for decades without any service.

The primary mirror cell was also reworked. The existing radial supports were found to be stuck as a result of corrosion. The repair required critical machining of some of the components to increase the clearance. The cell design also suffered from the lack of tip/tilt collimation screws. Although there were 36 counterweighted lever supports, there were no hard points to define the mirror axial position. Three of the counterweight assemblies were removed and replaced with suitable adjusting screws. Now the primary mirror is adjustable in tip/tilt and centring which allows the optics to be collimated.

With the worm gears un-meshed, the bearing friction was quite low in right ascension and declination and the difference in the bearing torque required to initiate movement and to continue movement, was also very low. These bearing friction values are key to providing a telescope that responds well to motion commands and points well. The mesh of both worm gears was set for minimum backlash and still operate over the entire motion range of the telescope. After extensive balancing of the telescope in four axes, the telescope slews and tracks satisfactorily.

The DFM Telescope control system makes provision for custom user interfaces through the use of callable routines, as well as the possibility to be remotely controlled through a manual switch selected start-up setting. The telescope control system can thus be used as a peripheral to a computer system, allowing integration with custom developed observing software. This is utilised to some extent in a newly developed camera control package, called *SPICA*, that utilises a visual interface to control the exposure times, read certain values of position and time from the DFM system, and automate the saving of images. A complete description can be found in paragraph 4.3.1. The specifications of the DFM telescope control system are described on the DFM webpage[19]. By utilising the software package, *The Sky*TM, one can do random point checks over the night sky. These point checks will have an initial offset, that is logged into the DFM system via the hand paddle. Typically a star will be chosen with *The Sky*, the move command initiated and when the telescope stopped moving, the star will have an arbitrary offset. This is rectified by moving the telescope with the hand paddle to the centre of the field of view. This offset is now noted on the DFM system as an offset. The DFM system thus creates a drive correction matrix for specific RA and DEC regions.

Extensive pointing measurements were also made with the telescope on both sides of the pier. The typical pointing is now better than 25 arc seconds RMS. If preload motors were added to the drives to remove the backlash, the pointing could be improved to about 15 arc seconds RMS.

3.2 Camera

The camera on the telescope is a thermoelectrically cooled 1024×1024 PixelVision CCD camera. It is used on the prime focus of the Cassegrain system. The box housing the camera is attached to a filter wheel, containing $UBVR_cI_c$ filters. These filters are described fully in section 5.4.

The camerahead contains a SiTe back-illuminated chip, with $24 \times 24 \mu$ pixels. The sensitive area is 24.6×24.6 mm. Full well capacity is 350,000 electrons with a maximum response non-uniformity of $\pm 5\%$ rms. The dark signal is 3 electrons/pixel/sec. The quantum efficiency of the chip is shown in fig 3.1. The plate scale of the CCD is calculated to be $8.59''/\text{mm}$, with a field size of $4.5'$. A new primary light shield was designed to provide an 80 mm diameter field to support the new CCD camera system that would be used on the telescope.

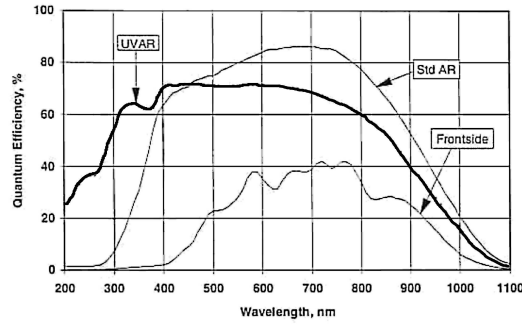


Figure 3.1: Quantum efficiency of SiTe chip used in PixelVision camera (UVAR) compared to front illuminated and the standard (Std AR) chips [34].

3.3 Filters

The filter wheel in use at the Boyden 1.5-m telescope contains the Bessel filters representing the Kron-Cousins system for R & I and the Johnson / Kron-Cousins definitions for U, B and V. The transmission curves for the various filters used at Boyden Observatory is shown in figure 3.2

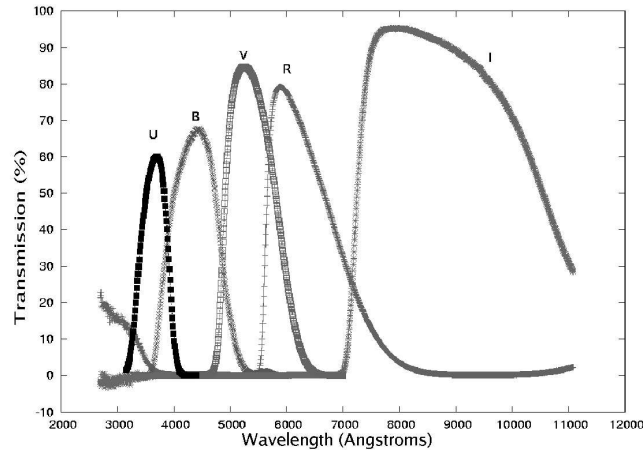


Figure 3.2: Filter transmission curves. Filter data from Kitt Peak Observatory.

Chapter 4

Camera Control and Image Acquisition Software

4.1 Observational requirements for system

A significant part of this study involved the developing of software that is in daily use at the 1.5-m telescope at Boyden Observatory. These programs are custom written for the systems and directory structures, and make use of the existing network layout . *Any changes to the directory structure, network parameters or hardware, may render these programs inoperative.* Small changes to the programs may solve these potential problems. All software developed during the study are available on CD-ROM, included in this thesis and backups are held at Boyden Observatory. Copyright for all material is held by Boyden Observatory.

4.2 Software

The wish list for the control program of the refurbished 1.5-m telescope included a few essentials. These were that the files should be named automatically allowing rapid saving and reducing time spend typing the file names. The files needed to be in FITS format with standard headers. The main problem to overcome before the program could be implemented was that Windows 2000TM do not allow direct use of the serial or parallel ports. After several attempts another demonstration section of a communication program was decided upon for use as communication medium. The DFM system allows communication through the Astronomical Control Language(ACL) routines. These routines are used via an agreement between Software Bisque and DFM, so that the commercial program *The SkyTM* can be used freely. Communication with the DFM computer was possible, and the data available through ACL could be read and utilised. The program development was done using Borland's Visual C++ (ver 5) environment. This made it relatively easy to implement the FITS libraries that were available. The final addition to the program was an option to scan an error box, enabling Gamma Ray Burst afterglow searches. There will inevitably be other updates to the program, like focusing, synchronising to known stellar databases, centering of the telescope, automatic identification and tracking of stars for photometry, etc. The program is described in section 4.3.1.

Rapid photometry has been identified as a high priority. The software from the Starlink project was available, evaluated and with the time at hand, implemented. Scripts were written in the tc-shell under Linux to enable interactive CCD reduction and photometry. The CCD reduction process with the scripts is normally done after the observing run. Photometry measurements can of course still be done during the run on individual images if bias frames and flats are available to use. The photometry process is carried out using standard stars. The process is part of this thesis and described in chapter 6.2.

The software used during the observing run consists of various programs that can be used in parallel. A brief description of each program is given in the sections under 4.3. These programs are on different computers in the control room. The names of the computers are

AURIGA The "charioteer" of the telescope, running PC-DOS. Supplied by DFM as part of the telescope control package.

BOOTES The "herdsman" of the data. Controls the camera and associated hardware (filter and autoguider) under Windows 2000. This is the only computer linked to the telescope controller via the DFM control program running on AURIGA.

MENSA The first locally supplied computer used for backups, data reductions, photometry and general work under Linux and Windows 98.

PAVO Showing off as a peacock, the fast, new Pentium is used for photometry and data reductions under Linux.

4.3 Camera and Filter Software

4.3.1 SPICA

This is the program utilized for the photometry research program of the Physics Department. Given the severe time constraints of photometric campaigns especially when the observer has to switch between sources on a regular basis per night, the package has been developed to limit the input from the observer to an absolute minimum. In fact, with the option of having an observation list to choose from, there is no need to type input at all. Tasks performed by SPICA are:

- The files are named automatically
- Objects are grouped according to *Project* and *Object* names, which are the directories used for the images
- Files are saved in the FITS format needed by the photometry scripts
- An automatic logbook is kept of all images saved, together with JD and airmass information.
- Up to 20 images can be taken in succession in a single filter band with interactive adjustments made to the exposure times
- A panning feature that will move the telescope is available to scan an area of up to 20×20 minutes, making for example the search for a GRB afterglow possible by scanning a satellite errorbox

- Saved images can be viewed in false colours with various image enhancing algorithms
- Editing of certain FITS header information is possible
- Utilising a text formatted file, targets as well as standards can be lined up with the appropriate filter and exposure settings needed

The program has several "tabs" that separate the different functions.

Initialization tab The only input required is the name of the observer and the observing file, if any. On the rest of the screen default values are used. A database of suitable standard stars as well as star fields identified with very dim stars that can be used for sky flats is available. Other databases for objects in the research program of the Physics department are also listed.

The user can generate custom databases with any text editor. The format of the file is:

PROJECT OBJECT RA DEC EPOCH FILTER EXPOSURE

The restriction on the coordinates is that it has to be specified in *hh mm ss* format. A typical file layout can be:

```
point 30_psc 00 01 25.3 -6 04 21 2000 C 1
var s_scl 00 14 51 -32 06 12 2000 U 500
standard hd2892 00 32 10.2 01 11 09 2000 U 90
standard hd2892 00 32 10.2 01 11 09 2000 B 90
standard hd2892 00 32 10.2 01 11 09 2000 V 90
standard hd2892 00 32 10.2 01 11 09 2000 R 90
standard hd2892 00 32 10.2 01 11 09 2000 I 90
var s_scl 00 14 51 -32 06 12 2000 B 350
.
.
.
```

Acquiring Images tab This is the main screen of the program where the data, filters, filenames, etc. are displayed. The object coordinates can be typed in, and are stored under OBJECT-RA and OBJECT-DEC in the FITS header. The program reads the current coordinates pointed to by the telescope from the DFM computer and displays it in a box marked TELESCOPE. An error message will appear if *The Sky* has a link open to the DFM computer, as both programs will try to communicate continuously using the same port.

The user has to enter a *Project* name and an *Object* name, together with the Epoch of the supplied RA and Dec coordinates. The telescope can be asked move to these coordinates. The coordinates can alternatively be typed on AURIGA. Notice that the coordinates displayed by AURIGA are the current Epoch coordinates as reported by the telescope. The exposure time and the number of images to be taken can be selected. The filter should be correlated with the ACE program's filter wheel setting. The filename will be shown as well as a window with the indicated directory file listing.

The user can choose between three types of images, namely Data, Bias and Flats. The differences are :

Data The coordinates of the center of field are read from AURIGA. Calculations are done to get the hour angle and airmass.

Bias The exposure time is set to 0.01 seconds. No data is read from AURIGA.

Flats The exposure time is as set by the user. No data is read from AURIGA. An additional data box with the average and standard deviation of the pixels on the image is shown for evaluation.

The images can be adjusted by three transformation settings. These settings are purely for the visibility of the images, and no changes here will be saved with the images. A small magnifying box is also available, with a marker assisting in marking positions on the image.

The marking for photometry on MENSA allows the user to select up to 20 stars that will be used to generate a light curve with the Starlink photometry software available on MENSA. *The first mark is used for the point-spread-function, so care should be taken in marking a well defined, uncontaminated star away from the edges of the field.* These marks can be moved during an exposure, as the exposure will be saved after the exposure is completed. The telescope may drift from exposure to exposure, and the incremental movement will allow the points to match the stars. With this option enabled, an additional position file will be saved with the same name as the FITS file. This file will be used in the photometry process. There are no changes made to the image file itself in marking positions on the image.

Examine Images tab Images can be viewed with various colour settings and display parameters. An option for deleting files is available.

Sweep Errorbox tab In searching for the GRB afterglows, the scanning of the errorbox is needed. After taking an exposure in the normal manner on the *Image Aquisition* tab, the user switch to this page, where the central image (center of field) will be displayed. The user can click on any position surrounding the image to get an exposure of that region of the errorbox. When the mouse is moved over an image, an enlarged image of the region will be displayed.

Edit FITS Header tab The appropriate headers can be edited and other headers added if needed.

Focus and Pointing tab Focus of the telescope is done by comparing successive exposures. Unfortunately several individual exposures grouped on a single image can not be done. This can however be achieved with software. The focus is done by choosing the lower and upper extremes for the focus potentiometer on the telescope. Five images will be taken equally stepped between these values. The telescope will be moved in a L-shaped path to make identifying easy of the various values used. This can be repeated as needed.

4.3.2 Other software

Pixelvision

This program is a standard "demo" program that came with the Pixelvision camera. This program is utilized for the following :

- focus
- pointing
- camera resetting
- general image acquisition

The full description of the program is contained in the manual which is available in the control room.

The Sky A planetarium program with a telescope control interface on the serial communication port. This program actually can't be used in parallel with SPICA as both programs utilize the same communication port. This program can be used to initialize the telescope, set the pointing accuracy and move the telescope to any object available in its database. The full description of the program is available in the comprehensive help screens available in the program.

ACE This is the program that controls the filter wheel and the position of the autoguider.

STV Remote This is the interface for the control of the autoguider. It is basically just a copy of the guider computer located at the bottom of the telescope. The manual for this program is also available in the control room.

4.4 Current status of the telescope

The official DFM upgrade was also complemented by additional problems that had to be ironed out before the the telescope could be used fruitfully in the research programme. This is illuminated in the next sections.

The photometry done at the telescope is influenced by several factors. Any defect in the telescope optics will adversely affect the photometry outcome. There were mainly five serious problems that were addressed as part of this study.

4.4.1 Aluminizing of mirrors

Both the telescope mirrors needed re-aluminizing. The primary mirror was alluminized by the staff of SAAO (South African Astronomical Observatory) in Sutherland during April 2003. The secondary is in a rather poor condition and plans are underway to alluminize this mirror as soon as possible.

4.4.2 Electronic noise

A varying periodic noise signal became more pronounced as time progressed. This signal was added at the end of the image aquisition, and stayed the same no matter what the exposure time

setting was. A number of possible causes were investigated, but in the end, all possible influences from the telescope and electronics in the dome were eliminated, leaving only the camera controller electronics as the culprit. The problem was pinpointed to the AD converter card, located in the camera controller. This noise was thermally linked and seemed to come from defective parts. As the camera controller manufacturer, PixelVision, was no longer in business, the only option left was to obtain a new camera. At the time of writing, no camera has been purchased yet.

This noise can be seen as a frequency present in the bias frame and the distribution graph (fig. 4.1).

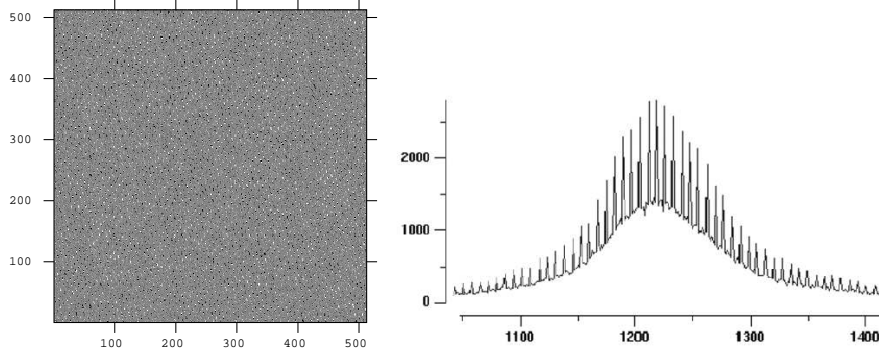


Figure 4.1: Bias frame showing the effects of electronic noise and pixel value counts against count distribution shows clearly the periodic noise present in all the bias frames. This noise is present in all the images as well.

4.4.3 Electronic and mechanical failures

The camera contained a faulty power supply, and after fixing this, the camera attained a temperature of 215-220K, almost 15K cooler than previously obtained temperatures. It was also found that the shutter on the camera is stuck and gets stuck each time it is loosened again. This accounts for the slope in the flat fields that was seen. Typically under middle-of-the-night flats, taken on sparse starfields, the problem was minimised. The results are shown in fig. 4.2.

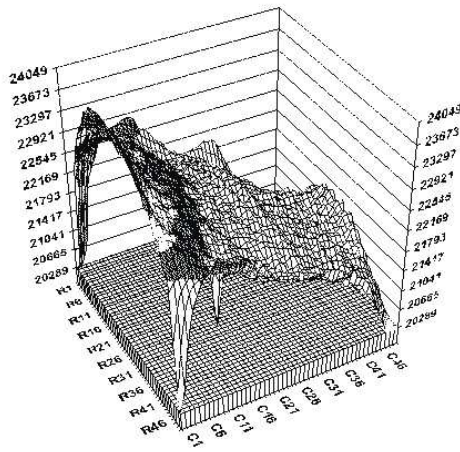
Until the problem with the shutter is solved, no accurate measurements can be made using either point-spread-functions or differential measurements. Results of the different methods can be seen in paragraph 7.1.3. It is possible with advanced knowledge of IRAF to model the flat field and apply the modelled flat field. This option is not explored in this thesis.

4.4.4 Collimation

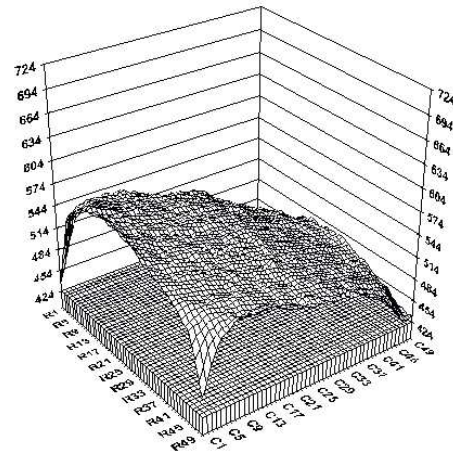
Collimation of the primary and secondary mirrors was a serious problem. Poorly collimated mirrors produce out-of-focus images. The Hartman screen can be used as a tool to test collimation. The Hartman screen used for image evaluation at Boyden is shown in fig 4.5.

4.4.5 Baffles

Decent flat field images were difficult to obtain as the scattered light in the dome and telescope fluctuated continuously. The dome has windows all around, allowing scattered light to enter the



(a) Twilight flat field profile



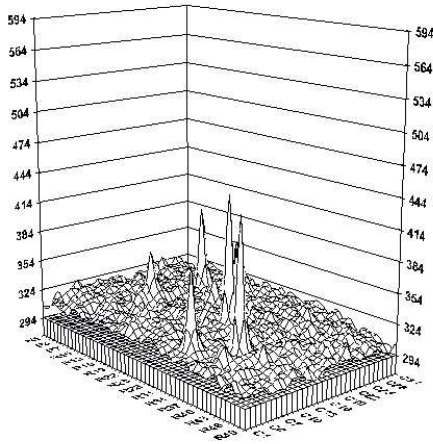
(b) Night sky flat field profile

Figure 4.2: Profiles of flat fields at Boyden taken at twilight and during the observing run on sparse starfield.

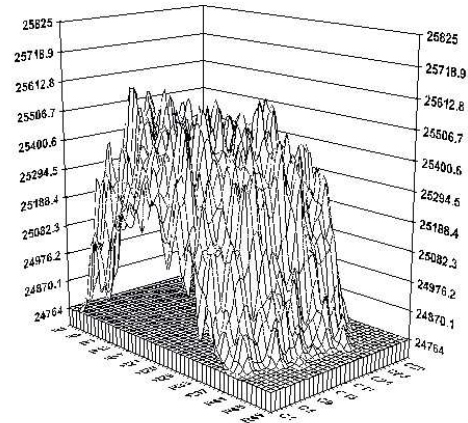
telescope. The problem can be seen if comparing a typical image, flat and flat fielded image (fig. 4.3) with that obtained at Boyden (fig. 4.4). The problem is partly corrected for by fitting rings in the baffle of the primary mirror.

The original baffle on the primary mirror is too short to exclude all the light from the sky. The effect of this on the image was clearly shown by placing a pinhole in one of the empty slots on the filter wheel. The pinhole basically shows the inside of the telescope and consequently also all reflecting surfaces. Figures 4.7 shows the light profile before and after installing a better baffle system. Clearly there are a lot of noise in the system, and a new baffle was needed. The only solution was to take flats during the night using a sparse starfield is shown in figure 4.2. Clearly from these images it can be seen that the flat fields actually "hides" the stars, instead of adding to their visibility! This presents a serious problem concerning the photometric measurement of stars on these images. No compensation can be obtained via flat fielding for dust and scratches present on the filters or the optical window of the CCD camera.

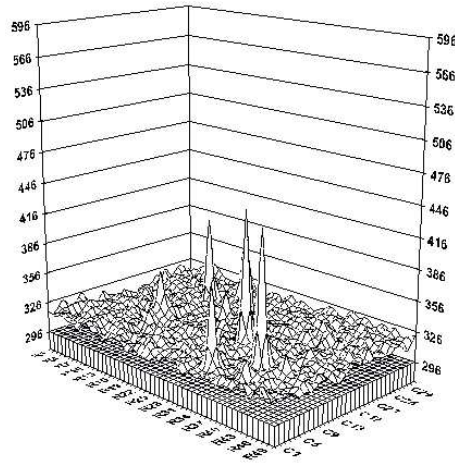
Considering all these problems, it was decided to replace the old baffle with a longer baffle. The longer baffle however, would require a new telescope cover to be made. To save time a compromise on the length of the baffle was made with a set of four rings inside the existing baffle that effectively blocks any stray light (fig 4.6). The image quality was remarkably improved, and the pinhole image of the new baffle setup compared to the image before the rings were introduced (fig 4.7), shows the result clearly.



(a) Typical raw profile



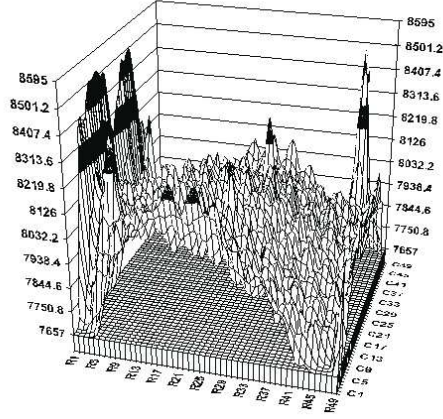
(b) Typical flat profile



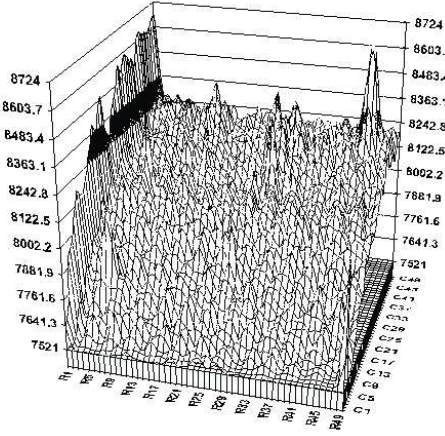
(c) Typical flat fielded profile

Figure 4.3: Typical profiles of a raw image, a flat field and flat fielded image.

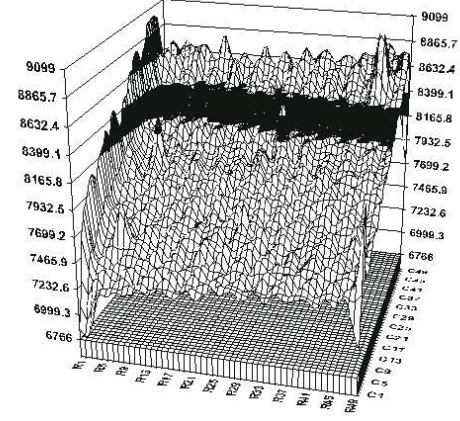
PKS2155-304_001_l.fit



(a) Raw image profile



(b) Flat fielded profile using twilight flat



(c) Flat fielded profile using nightsky flat

Figure 4.4: Profiles of a flat fielded image at Boyden flat fielded with the twilight and night sky flat fields respectively.

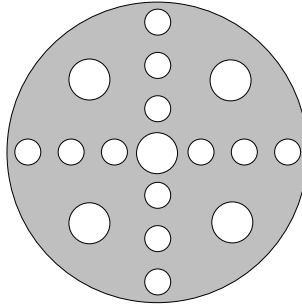


Figure 4.5: Hartman screen used for collimation of 1.5-m telescope.

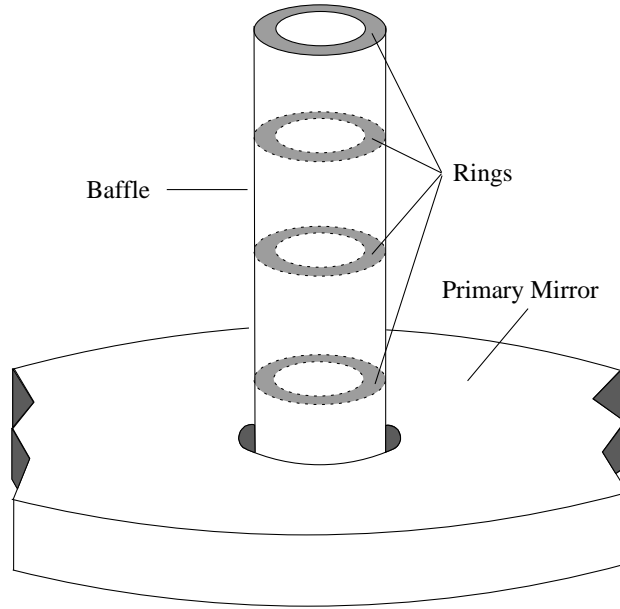


Figure 4.6: Drawing of the new baffle setup showing the four rings inside the old, shorter baffle. The rings are not to scale. The size of the rings were optically chosen to exclude all of the area visible around the secondary baffle.

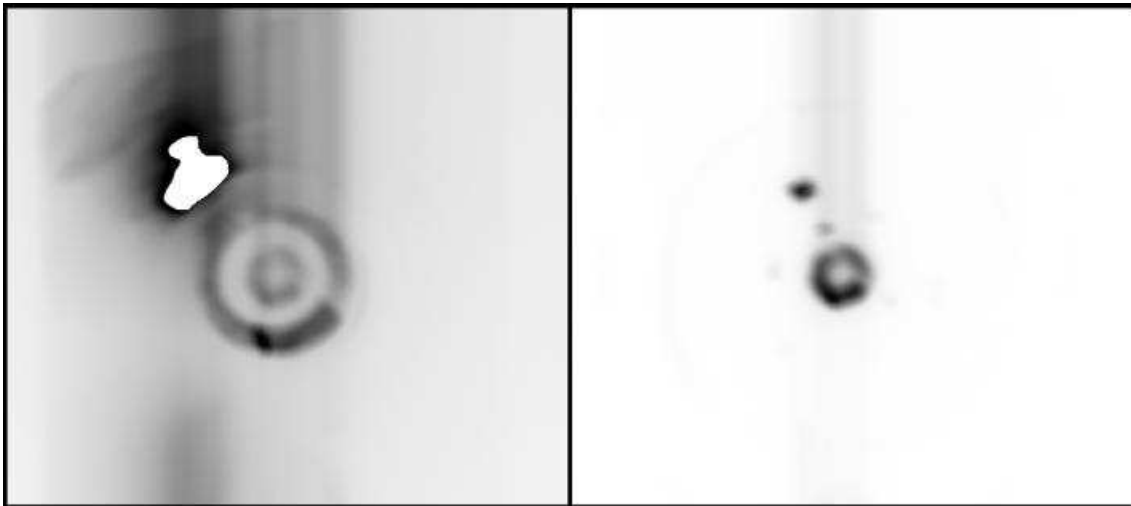
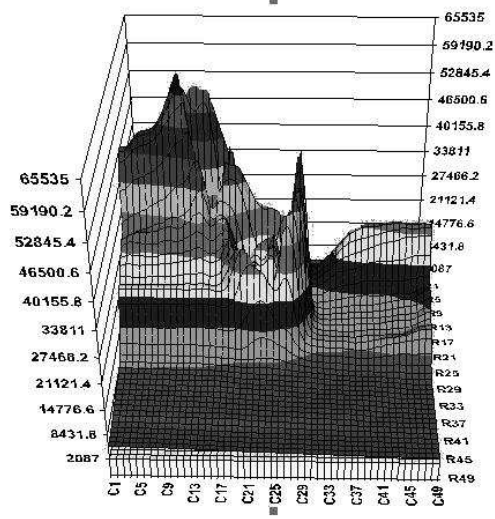
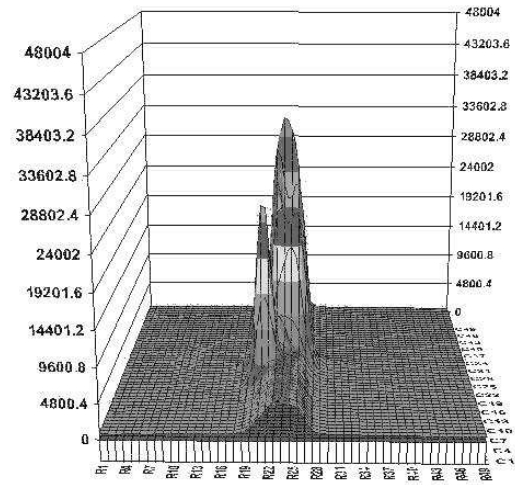


Figure 4.7: Comparable pinhole images of the inside of the telescope tube, showing a very bright, off-axis light source. The image on the left is before the rings are installed, the image on the right after the installation.



(a) Before installation



(b) After installation

Figure 4.8: Light profiles before and after adding rings to the baffle. The secondary peak is due to a bright off-axis light source placed for evaluating reflection elimination by the rings in the new baffle.

Chapter 5

CCD Images

5.1 Origins of Photometry

Originally, "astronomy" meant position measurement of the stars. The precise brightness of the stars was of lesser importance than their positions in the sky. After the development of the telescope, precise star brightness measurements gained importance with its application to variable stars. Any historical survey of stellar magnitudes begins with the work of Hipparchus of Nicea, who lived in the 2nd century BC. He divided the stars into six brightness classes called magnitudes. The brightest stars belonged to the first class, while the faintest were assigned to the sixth class. As the nineteenth century began, astronomers were on the verge of converting the magnitude steps of Hipparchus into a different system—that of a continuous scale of magnitudes. The greatest obstacle to this change was determining the zero point of the scale. A problem arising from the use of this scale system was to determine which stars of, say, the fourth magnitude class are 4.0 and which ones are 4.9. The average of the fourth magnitude stars would not be 4.5, since there are more stars at the faint end of the class than at the bright end. The definition of the exact 4.0 point became thus extremely important. A well detailed discussion is done by Zissel [44] dealing with the history of photometry.

The modern era of stellar photometry began with Argelander (1799-1875), who introduced the "Step Method" of estimating magnitudes. This method uses a brighter and fainter comparison star to bracket the variable. The interval is divided into a convenient number of steps. Argelander's first results were published in 1843 in a paper on the light variations of δ Cep, β Lyr, and η Aql. The brightness is not given in magnitudes, but in intensity, called "Grades." The important concept introduced in this paper is that the brightness units were given on a continuous scale to one decimal place. In his later publications, Argelander transformed his brightness grades into magnitudes that were related to those of Hipparchus. The faintest third magnitude and brightest fourth magnitude stars of Hipparchus became magnitude 4.0. Argelander's successor at Bonn, Schönfeld, continued the work down to -24° declination. In 1885 Thome' went to Cordoba, Argentina, to extend the survey to -62° . The various works, collectively known as the DM, contain 579,000 stars and were of great importance to the advancement of stellar photometry studies. The DM were based on eye estimates which varied with observer colour sensitivity and fatigue. A better method of photometry was needed to actually measure the brightness rather than just estimate it.

In 1836 John Herschel used an "astrometer" to compare the brightness of stars to a reduced image of the moon. This was a true photometer, in that it contained a scale to read the brightness, and that one could compare equal intensities rather than estimating intensity intervals. An inaccurate theory of moon-brightness as a function of phase limited its usefulness, along with it being able to measure only the brightest stars, since it could be used only while the moon was in the night sky. An artificial star formed by a lamp flame and a pinhole was projected into the telescope field of view. The brightness of this image could be attenuated by rotating one of a pair of polarising prisms. The intensity changes in proportion to the square of the cosine of the angle of rotation between the prisms. By alternately matching the artificial star to two stars in the field, one could determine the brightness ratio of the two stars, i.e. differential photometry. As long as sky transparency remained constant, one could even compare stars in adjacent fields or in different parts of the sky. The Zöllner photometer was invented before the age of the electric light. One disadvantage was the use of a flame for the light source. The flame was always vertical and flickered in a slight breeze, while the photometer could be in any orientation at the eyepiece as the telescope pointed to various parts of the sky. Another disadvantage was the appearance of the artificial star. It did not appear the same as the real star since it did not undergo the effects of seeing. It is difficult to tell when both images are the same brightness when they have different appearances.

When Argelander visually produced the BD catalog he assigned magnitudes to the stars recorded to one decimal place. The magnitudes roughly followed Hipparchus's steps. The significant difference being that Argelander's system used continuous real numbers while Hipparchus's was quantized in integers. The Harvard Photometry project by Pickering used a measuring device to perform photometry on four thousand stars. He defined the zero point of the Harvard system by observing a number of stars in the fifth magnitude range from the BD each night and assuming their average magnitude. Thus, the systems were tied together by the average of many stars; not by a single star.

Obviously astronomical photometry came a long way since these early years, but still a lot of problems remain. Some of these problems are dealt with in this study, but photometry in this study is discussed and used as a means to an end: the use of photometry is implemented in the form of various scripts to make observations and subsequent measuring of magnitudes of rapid variations in flaring systems at Boyden Observatory, as well as allowing photometric studies of microlens and GRB afterglow events.

Of course the development of photography and the use of density measurements for photometry purposes and the use of photomultiplier tubes (PMT's) must also be mentioned. PMT's were sensitive to the blue end of the visible spectrum, but due to the material used for photon multiplication, not very sensitive to the red end of the spectrum.

5.2 CCD technology

The main advantages of CCDs are their sensitivity, dynamic range and linearity. The fraction of photons, falling on the chip, that are detected or registered, is termed the sensitivity, or quantum efficiency of the chip. Average quantum efficiencies of around 80% is common to most modern CCD's. This can be compared to typically only a few percent for even cooled sensitised photographic plates. CCDs are responsive to a broader range of wavelengths and are much more sensitive

to red light than either photographic plates or the photomultiplier tubes used in photoelectric photometers. However, they have a poor response to blue and ultra-violet light.

CCDs are sensitive to a wide range of light levels. For example, a typical dynamic range is about 10^5 , corresponding to a range of about 14.5 magnitudes. A photographic plate have a range of less than about 1000, corresponding to 7.5 magnitudes[12]. This dynamic range of the CCD is essentially linear, i.e. the size of the signal is simply proportional to the number of photons detected; calibration is thus straightforward.

A disadvantage of a CCD is the physically small size. It can image only a small region of sky. Typical sizes are much smaller than photographic plates. To enable an observer to image a larger area in the the sky, several chips can be used as a mosaic. There is a practical limit though to the size of image obtained, due to the time required to read it out.

5.2.1 Pixel size and field of view

The small size of the CCD chip used, and the fact that the chip is on or near the optical axis, there is a linear relationship between angles subtended on the sky and distances on the CCD. The plate scale is defined by

$$p = \frac{\Delta''}{\Delta mm} \quad (5.1)$$

where p is the plate scale in *seconds of arc per mm*, Δ'' is a displacement on the sky in *seconds of arc* and Δmm is the corresponding displacement in the focal plane in *mm*. The plate scale can also be derived from the parameters of the telescope by using

$$p' = 1/f$$

where f is the effective focal length of the system and p' is the plate scale. The units for the plate scale will then be *radians/focal length units*. The angle subtended by each pixel can be determined from

$$\theta = s/f$$

where s is the pixelsize in *mm* and f is the focal length of the system in *mm*. The focal length is simply related to the diameter of the primary mirror, D , and the focal ratio, F according to

$$f = F \cdot D \quad (5.2)$$

At larger distances from the optical axis there is no longer a simple linear relation between angular displacement on the sky and displacement in position in the focal surface. That is, p varies as a function of position in the focal plane. This effect is usually not important in instruments like the Boyden 1.5-m UFS Reflector, containing only a single chip of relatively small size. However it may become important if an array of chips are used.

5.2.2 Instrumental Effects in CCD Detectors

Bad pixels

CCD technology is however not perfect. Pixels on the CCD chip may be faulty and return signals which are inaccurate. Terms like ‘hot’, ‘cold’ or ‘bad’ are used to describe these pixels. Because pixels in a row or column are electronically linked to each other, contamination can lead to a complete row or column being bad.

Bias frames

In amplifying the signal before it is being digitised, a certain amount of noise is introduced. This is known as the bias that is added to the actual data. There will be a slight variation over the whole of the chip, and the variation may vary with time. Keeping a constant temperature may lower this variation. Usually there are two ways of determining the bias introduced.

Bias strips Images contain two narrow strips on either side of the chip where the bias and its noise are stored. Usually the row next to the bias pixels is averaged and the value is subtracted from the pixels in the actual data.

Bias frames When the entire chip is used to gather data, taking bias frames gives a frame that shows small scale structure in the noise. Corrections can be made easily. At Boyden several short exposures are used with the shutter closed before and after each observing run. These frames are then averaged and assembled into a ‘master bias frame’, that is used on the flats as well as the data.

The effect of adding a bias value to the amplification will cause the Analogue-to-Digital Converter (ADC) in the camera to always receive a positive value. The ADC is converting the signal representing the amount of charge accumulated in a CCD pixel to a digital value. The bias level has an intrinsic noise that is induced by the signal amplification, known as the ‘readout noise’. This is one of the features which limits the usefulness of CCDs at very low light levels.

Photon noise

For photon noise, there is no correction method. This is due to the Poissonian nature of counting photons. In this case the error in the signal is proportional to the square root of the signal.

5.3 Data Reduction

When dealing with data, photometric measurements of an object will be made without any knowledge of the defects that were present at the time of the data capture. During the data reduction stage, all defects present in the images will be removed. These defects include the noise that can be corrected for as well as deviations in the intensity over the frame. These changes should be noted in the FITS header.

It may be necessary also to apply registration, alignment, normalisation and combination. Registration is the process of determining the transformations which map the same positions on different datasets. This is essential if measurements, say with different filters, are to be made. In this case

registration may be informal and just consists of identifying the same objects on different datasets. However, very accurate measurements are often also required; certainly this is the case when data combination is to be performed. ‘Data combination’ is just when aligned datasets are combined by a process of taking the mean or some other estimator at each pixel, this is also frequently referred to as ‘mosaicing’. Aligning datasets means achieving pixel-to-pixel correspondence (in real data it is unlikely that this state is true, even if it was intended). Alignment uses the registering transforms to ‘resample’ the data onto a new pixel grid. If the exposure times, atmospheric transparency or sky brightness have varied, then data must be “normalised” before combination. Normalisation is the determination of the zero points and scale factors which correct for these changes.

While photometers only allow an indiscriminate collection of all light entering a diaphragm, CCD technology provides several stars on a single image, making differential photometry possible. The lack of any standard star on the image however, still prompts the use of separate images of standards for calibration.

Although this study did not attempt to develop any new photometric techniques, the differences and advantages of various photometric procedures that may be employed to do photometry, were studied and suitable methods decided upon afterwards for the observations at Boyden Observatory.

Flatfielding

The sensitivity of a CCD to incident photon flux is not uniform across the whole of its surface and before data is properly flux calibrated, this needs to be corrected for. The variations in CCD response can be on the large scale (one end of the CCD to the other) and pixel-to-pixel. Since the relative flux levels on different parts of the CCD are also vignetted by the optics of the instrument and telescope, this variation also needs correcting for and is performed together with the CCD sensitivity corrections.

Flatfield calibration frames are usually taken of a photometrically flat source using the same optical setup as that used to take the object frames. In the past images of the interior of the telescope dome have been used for this purpose, however, it is now generally thought that images of the twilight/dawn sky are more representative of a true flatfield, having the same global illumination as the global illumination as the object frame and having a comparatively good signal (noise) level uniformly distributed across the whole chip. Keeping in mind that these calibration frames will be applied to the object data at some stage and hence will introduce a random noise base to the final data values, it is therefore essential to get a good set of calibration frames with lots of signal. There is a problem however, in that these frames have a colour response which may be not representative of the colour of the night time sky. If this is important then night sky flatfields must be produced. These can be taken of star-free parts of the sky or produced from many object frames whose contaminating objects are removed, before median stacking is performed to remove more spurious data values.

Successful photometry is only possible after all the system parameters brought into the image have been accounted for. These include vignetting, electronic noise, absorption due to dust, filter corrections, cosmic ray events and the exposure time of the image. Taking a good flatfield is essential

for displaying very dim objects. Dim in this regard means any brightness that is slightly above the background brightness of the image. The flatfield will also correct for pixel non-uniformity, vignetting and dust spots. Any light variations over the image will also be picked up by the flatfield image. It is possible to combine different sorts of flatfields to obtain the advantages of each. For example, you could use dome flats to correct pixel-to-pixel sensitivity variations and twilight flats to correct large-scale effects such as vignetting. For the 16-bit camera in use at Boyden, a mean pixel count of around 20 000 out of a possible 32 767 is used for optimal effect.

Fringing

In the case of observations made through a narrow-band filter, or where the incident light contains a strong component at a single wavelength, multiple reflections within the CCD chip, or the filters in front of it, can cause wave-like patterns across the image. These patterns are called fringes. The precise pattern depends strongly on the exact wavelength of the illuminating light. Consequently, correcting for fringing requires a flatfield whose wavelength corresponds closely to that of the image.

The fringe pattern is an additive effect and must be subtracted. To remove fringes it is necessary to obtain several exposures of either a region of night sky containing no objects or, alternatively, remove all the contaminating objects from data frames which otherwise contain large areas of night sky. These frames should then be combined to give complete spatial coverage and to reduce the noise contribution. The resulting fringe-frame should be scaled to the fringes present in the data frame, after normalisation, and subtracted.

The emission from the night sky usually includes narrow emission lines originating in the terrestrial atmosphere. These lines will often fall within the bandwidths of broad band filters. However, they are not present in the featureless spectra of dome flats. Consequently dome flats may not be appropriate when fringing due to night-sky lines is present.

Cosmic-ray events

Spurious signals in CCD frames caused by ionising radiation is termed cosmic-ray hits or cosmic-ray events. However, these ionising events are as likely to be due to background terrestrial radiation as cosmic-rays. When a cosmic-ray particle hits a CCD pixel it causes an increase in charge which is indistinguishable from the arrival of photons. These spurious signals are usually, though not always, confined to single pixels. Cosmic-ray hits appear as a set of pixels with intense values sparsely scattered over the CCD frame. Typically an exposure of a few minutes might have about a hundred cosmic-ray hits. The location of the hits within the chip is random. If several frames of the same target object or flatfield have been acquired then the cosmic-ray hits will occur at different positions in each frame and it is possible to detect and remove them by comparing corresponding pixels in the different images and rejecting those with aberrantly large values.

Dark frames

All CCDs, at some level, exhibit the phenomenon of dark current. This is basically charge which accumulates in the CCD pixels due to thermal noise. The effect of dark current is to produce an additive quantity to the electron count in each pixel. The reduction of dark current is the main reason why all astronomical CCDs are cooled to liquid nitrogen temperatures. Most modern CCDs

only produce a few ADU¹ (or less) counts per pixel per hour and so this effect can generally be ignored. This, however, is not the case for Infra-Red arrays.

The electronic noise caused by the thermal radiation of the CCD chip and camera assembly, as well as other constant noise patterns like the readout noise, can be subtracted from the image by taking a dark frame. This must be done at the same operating temperature as the image. This is especially useful with longer exposure times. At Boyden this is not done, as the camera is cooled with a thermo-electric cooler to a temperature around 50° below the ambient temperature.

5.3.1 Data Reducing Procedure

The reduction procedure is not trivial, and it must be carried out carefully. Typically one would:

1. inspect the original images and discard those that are faulty,
2. flag all the known faulty pixels as ‘bad’ or replace them with invented, reasonable values,
3. create ‘master’ bias images for subsequent use in removing the bias signal from raw images of the target astronomical objects,
4. for each filter, create a master flatfield frame defining the pixel-to-pixel sensitivity variations and then flatfield each of these images,
5. if necessary, for each filter, align and add the individual images of each target astronomical object to produce a master image of the object.

5.4 Photometric Systems

The existence of various photometric systems are linked to the filter sets used in the observations that one performs. The intensity measured with any system is influenced by the varying responsiveness of different wavelengths of the detector. For example visual intensity levels as seen by the eye, peak in response around 5500 Å. This is different for CCD detectors, which peaks normally around 7000 Å, while the peak sensitivity of PMT’s is around 4500 Å [34]. Modern photometric systems are defined for photoelectric and CCD detectors. A photometric system is described by a set of discrete wave-bands, each with a known sensitivity to incident radiation. The sensitivity is defined by the detectors and filters used. A set of primary standard stars exists for each system as a definition of its magnitude scale. Passbands for filters are defined as wide (at least 300 Å wide), intermediate (between 300 and 100 Å) and narrow (a few tens of Å wide).

Johnson-Morgan (UBV) System

The Johnson-Morgan photometric system for the U, B and V filters was chosen with a zero point where a star of spectral type A0 would have in the absence of interstellar reddening, $U = B = V = 0$. This system was introduced initially to be used with photomultiplier tubes. The tubes had a strong response in the blue and very little in the R and I bands. The system started in the 1950’s with only the UBV bands, with the R and I added later. See chapter 5.1 for more detail on the origin of the photometry systems.

¹ADU (Analogue-to-Digital-unit) This is the digital count representing the amount of electrons liberated by the CCD pixel for each photon that falls on the chip. This is linked to the gain and quantum efficiency of the CCD chip.

Cousins (UBVR_CI_C) System

This is basically an add-on to the Johnson-Morgan system, with southern data for the R and I bands. The Cousins *V* band, complemented by *U* and *B*, are identical to the Johnson-Morgan system. However, the Cousins *R* and *I* bands respectively have wavelengths of 6700 Å and 8100 Å and thus both are bluer than the corresponding Johnson-Morgan bands (see Table 5.1). These bands are indicated by (*RI*)_C, where ‘C’ stands for ‘Cape’. The *UBV* system has some disadvantages. In particular, the short wavelength cutoff of the *U* filter is partly defined by the terrestrial atmosphere rather than the detector or filter. Thus, the cutoff, and hence the observed magnitudes, can vary with altitude, geographic location and atmospheric conditions.

Johnson (UBVRI) System

This can be considered to be the ”standard” and most widely used photometric system. This system was however originally developed for PMT use with strong blue response, with very little red sensitivity.

Strömgren System

The Strömgren intermediate-band *uvby* system is also widely used and the Strömgren *y* is well-correlated with Johnson-Morgan *V* magnitudes.

JHKLM System

The *JHKLM* system is an extension of the *UBV* system to longer wavelengths in the near infrared. These bands are matched to, and share the same names as, the windows in which the terrestrial atmosphere is transparent at infrared wavelengths. The *L'* band is a later addition. It is better matched to the corresponding atmospheric window than the original *L* band [33].

The *JHKLM* system is less well-standardised than other systems and often local systems will be defined which differs slightly from that used at other locations. These differences arise because the atmospheric windows which are transparent at infrared wavelengths are themselves different at different observatories and vary with altitude. Great care should be taken in comparing *JHKLM* observations made at different observatories.

As for the original Johnson-Morgan system, the zero point of the *JHKLM* system is defined so that an unreddened A0 star has the same magnitude in all colours:

$$J = H = K = L = M (= U = B = V).$$

The standard star used is Vega (α Lyræ).

Kron-Cousins System

The arrival of CCD detectors made observations in the red and blue bands equally possible. A photometric system that can take the spectral response of the chip into consideration was needed. The Kron-Cousins UBVRI takes advantage of the CCD’s excellent response in the red and near-infrared region of the spectrum. Because of the CCD’s abundant near-infrared response, the U, B,

V and R filters are carefully masked to prevent infrared 'leakage' which could skew the measurements.² Wavelength characteristics for the different filters are listed in table 5.1

| System | Band | Effective Wavelength | Bandwidth (FWHM) |
|----------------|----------|-------------------------|---------------------|
| | | Å | Å |
| visual | m_v | ~ 5500 | - |
| photographic | m_{pg} | ~ 4250 | - |
| Johnson-Morgan | U | 3650 | 680 |
| | B | 4400 | 980 |
| | V | 5500 | 890 |
| | R | 7000 | 2200 |
| | I | 9000 | 2400 |
| Kron-Cousins | U | 3600 | 700 |
| | B | 4400 | 1000 |
| | V | 5500 | 900 |
| | R | 6500 | 1000 |
| | I | 8000 | 1500 |
| Strömgren | u | 3500 | 340 |
| | v | 4100 | 200 |
| | b | 4670 | 160 |
| | y | 5470 | 240 |
| $JHKLM$ | | μm | μm |
| | J | 1.25 | 0.38 |
| | H | 1.65 | 0.48 |
| | K | 2.2 | 0.70 |
| | L | 3.5 | 1.20 |
| | L' | 3.8 | 0.6 |
| | M | 4.8 | 5.70 |

Table 5.1: Details of common photometric systems.[33]

²The Boyden telescope make use of this filter system.

Chapter 6

Photometry using CCD Images

6.1 Instrumental Magnitudes

To be able to measure the pixel counts in a CCD frame, the instrumental magnitude is used. The instrumental magnitude, m_{inst} , is defined as:

$$m_{\text{inst}} = A - 2.5 \log_{10} \left[\frac{(\sum_{i=1}^n C_i) - nC_{\text{sky}}}{t} \right] \quad (6.1)$$

where:

A is an arbitrary constant instrumental magnitude,

C_i is the count in the i th pixel inside the aperture,

C_{sky} is the average count in the background sky pixels,

n is the number of pixels in the aperture,

t is the integration time of the frame.

The instrumental magnitude is thus computed from the sum of the pixels inside the aperture with the average sky background subtracted. There are various ways of measuring the average. Using a simple mean value would not be acceptable, because of contamination of the chosen region by faint stars. Techniques are often used which minimise the effects of exceptionally high values in the sky background histogram, such as computing the median instead of the mean. One is to use an aperture positioned on a neighbouring region of blank sky, another is to use an annulus surrounding the original aperture. This is perhaps preferable as the true difference between the background and the star can be determined more accurately. Though the details of the point-spread-function fitting technique used in optimal photometry are very different, the definition of the instrumental magnitude is the same.

6.2 Different Methods of Photometry

6.2.1 Differential Photometry

By far the most accurate photometric measurements obtainable, is through the use of differential photometric measurements. Differential photometry is done by comparing instrumental magni-

tudes, or measured counts of two or more stars on one CCD field with each other. No need for calibration of the images is necessary, with reduction the only process to be done on the image. The main disadvantage of this method is that you must have a suitable non-variable star with known properties on the same field as the observed object. With the small field of view of the CCD detector this is very seldom obtained. Using a few stars on the field as "standards", most of the variable effects of a single star due to sky conditions may be corrected. Except if a known "standard" on the field can be used as reference, differential photometry provides no standard magnitude, but rather an instrumental magnitude and magnitude difference. This may be the only choice of doing any photometry on partial cloudy nights.

6.2.2 Aperture Photometry

The principle of aperture photometry is simple. For the star which is to be measured a circular region (or 'aperture') of the CCD frame is defined which entirely encloses the image of the star, that is, all the light from the star falls inside the aperture. This is very similar to the technique carried out with a single-channel photoelectric photometer. A circular aperture is placed in front of the photomultiplier to limit its view of the sky. Using software to define a circular region in a CCD frame mimics the effect of a physical aperture, limiting the field of view of a single-element photometer. The flux in all the pixels inside the aperture is added to give the total flux. A similar measurement is made of a region containing no stars to give the flux from the background sky. The two are then subtracted to yield the flux from the star. The same principle may be applied to extended objects such as galaxies or nebulae, though here an elliptical aperture may be needed.

6.2.3 Photometry from Image Profiles

A very effective technique to measure the magnitudes in crowded star fields is by way of point spread functions. In such regions the images of individual stars may overlap and it is impossible to position an aperture that simultaneously includes all the light from a given star and excludes all the light from its neighbours. Stars are, of course, unresolved by a conventional telescope and the star images recorded in a CCD frame simply trace out the point-spread function of the telescope. The point-spread function should be independent of the position of the star in the focal plane, at least for positions close to the optical axis. The point-spread-function fitting technique makes the assumption that all the star images have the same shape. Since CCD detectors are usually positioned on the optical axis and have a small field of view this assumption is valid. The light distribution in the CCD frame is modelled by assuming positions and brightnesses for the observed stars and knowing the point-spread function. This can be measured using isolated stars. The positions and brightnesses of the stars are iteratively varied until the observed light distribution in the CCD frame is reproduced. It is possible to perform accurate photometry of crowded regions using point-spread function fitting. It is important that all the images should have the same profile for this technique to be useable.

6.3 Sky Brightness

The signal to noise ratio (S/N) is the electronic counts of the stellar image relative to the counts in the sky background of an astronomical object. This ratio is decreased by a bright sky background

count. To determine the limiting magnitude due to sky background, the FWHM¹ of a star of known magnitude for a specific colour band must be determined. The point-spread-function (PSF) is the shape of the CCD image of an unresolved point of light, i.e. a star, has a distribution curve that eventually falls to zero, although it never reaches zero on the image plane. A cut-off point of the PSF that includes most of the stellar signal and not too much of the sky background is an annulus of measurement about 2 – 3 times the FWHM of the star image. The sky brightness in a $1 \times 1 \text{ arcsec}$ field can now be determined. The counts on the sky background, excluding any stars can be measured and normalized to 1 arcsec^2 . The sky background can be calculated using

$$m_{star} - m_{sky} = 2.5 \log_{10} \frac{B_{sky}}{B_{star}}.$$

The pixel counts (B_x) is not a true measure of magnitude, but using the ratio eliminates all the influencing factors from the CCD, etc. The sky brightness changes throughout the observing run, and factors like clouds, moonlight and local atmospheric turbulence can adversely influence the limiting magnitude that can be obtained. This in turn will of course influence the S/N that can be obtained and a good S/N is important for good photometry.

6.4 Air Mass

The path length through the atmosphere is the **air mass**. For any particular wavelength, λ , we can relate $m_0(\lambda)$, the magnitude of the observed object outside the atmosphere, to $m(\lambda)$, the magnitude of the observed object at the surface of the earth, by:

$$m(\lambda) = m_0(\lambda) + \kappa(\lambda)X(z) \quad (6.2)$$

where $X(z)$ is the air mass, $\kappa(\lambda)$ is the **extinction coefficient** at wavelength λ and z is the zenith distance. X is defined as the number of times the quantity of air seen along the line of sight is greater than the quantity of air in the direction of the zenith and will vary as the observed line of sight moves away from the zenith, that is, as z increases. The air mass is a normalised quantity and the air mass at the zenith is defined as one.

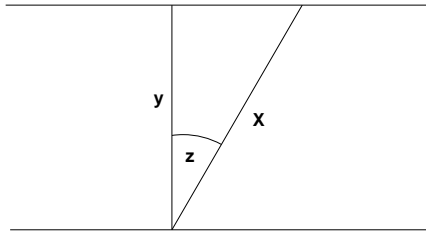


Figure 6.1: Schematic diagram of extinction.

From figure 6.1 follows that $\frac{y}{X} = \cos z$ and thus $X \propto \sec z$. For small zenith angles $X = \sec z$ is a reasonable approximation, but as z increases, refraction effects, curvature of the atmosphere and variations of air density with height can become important. This relation will limit to infinity at the horizon, and therefore Hardie[22] gives a more refined relationship:

$$X = \sec z - 0.0018167(\sec z - 1) - 0.002875(\sec z - 1)^2 - 0.0008083(\sec z - 1)^3 \quad (6.3)$$

¹Full width half maximum: the angular size of the star image at half the maximum peak value

Hardie's equation is the relation used at Boyden Observatory in the DFM control system programming. Young and Irvine[43] propose:

$$X = \sec z (1 - 0.0012(\sec^2 z - 1)). \quad (6.4)$$

Both these equations imply the use of z_t , as the true zenith angle. That is the zenith angle to the observed object in the absence of the atmosphere as opposed to the apparent zenith angle z_a affected by refraction effects. The atmospheric extinction coefficient, $\kappa(\lambda)$, is determined by observing the same object several times during the night at varying zenith angles. The **observed magnitudes plotted against computed air mass** should lie on a straight line with a slope equal to $\kappa(\lambda)$. It is important to note that the extinction is dependent upon wavelength, being greater for blue light than red.

6.5 Calibrating Instrumental Magnitudes

Calibrating instrumental magnitudes will transform the magnitudes obtained to standard magnitudes as observed in the photometric system. Calibrating instrumental magnitudes consists of correcting two effects namely

- eliminating the discrepancies between the instrumental and target standard systems and
- correcting for atmospheric extinction.

Instrumental effects influence the magnitudes obtained, and calibration is done assuming one of two scenarios, the instrumental system is well-matched to the target standard photometric system or the instrumental system is less well matched to the standard system. In the first case the detectors and filters used have been chosen carefully to match the responses of the target standard system as closely as possible. Thus, for example, the transmission profiles of an instrumental *UBVRI* system would be similar to those for the standard system.

Certain programmes does not neccitate the calibration of instrumental magnitudes , e.g. determining the periods of a variable star. It would of course still be necessary to correct for atmospheric extinction.

6.5.1 Calibration without a colour correction

Because magnitudes are logarithmic quantities and the standard and instrumental systems are assumed to be well matched, the principal difference between them is a zero-point correction. In this case the relation between instrumental and calibrated magnitudes is of the form:

$$m_{\text{calib}} = m_{\text{inst}} - A + Z + \kappa X \quad (6.5)$$

where:

m_{calib} is the calibrated magnitude,

m_{inst} is the instrumental magnitude (measured),

A is an arbitrary constant which is often added to the instrumental constants,

Z is a photometric zero point between the standard and instrumental systems,

κ is the atmospheric-extinction coefficient,

X is the air mass (known).

The equation can be rewritten as

$$m_{\text{calib}} - m_{\text{inst}} = (-A + Z) + \kappa X \quad (6.6)$$

This equation is a simple linear equation that can easily be solved using the known values for X and m_{inst} . It is not necessary to solve for both the constants A and Z , but rather treat them as a single constant. The published values for the standard stars are known as m_{calib} . Plotting $m_{\text{calib}} - m_{\text{inst}}$ against X for known standards will produce a straight line plot. The slope corresponds to κ and the y-intercept gives $-A + Z$. Substituting these values into the same equation for the programme objects leads to a corrected, calibrated photometric magnitude.

Thus by observing a standard star repeatedly throughout the night, a table of instrumental magnitudes can be produced that can be plotted against the air mass. Observations of the programme objects will be interspaced with observations of standard stars. Finally Z and κ can be solved for using least squares or some similar technique.

Because of the dynamic nature of the atmosphere, it is safe to do photometry on a (variable) programme star as well as one or more stars randomly chosen from the same frame to eliminate any variations in atmospheric extinction. When the seeing deteriorates, it is best to have this illustrated with a star of "constant" magnitude instead of interpreting it as a variation of the programme object.

6.5.2 Calibration with a colour correction

Calibration with colour corrections is usually appropriate in two cases:

- where the instrumental system is not well matched to the target standard system or,
- where very high precision photometry is being carried out and even small discrepancies between the instrumental and target standard systems must be corrected for.

Calibration with colour corrections is similar to calibration without a colour correction. The calibrated magnitude is still computed from the instrumental magnitude in the corresponding band in a manner similar to equation 6.6. An additional term is added corresponding to a colour index determined from an adjacent band. This term compensates for the mismatch between the instrumental and standard systems. For the Johnson-Morgan *UBV* system the calibration formulae are:

$$\begin{aligned} U &= U_{\text{inst}} - A_u + Z_u + C_u(U - B) + \kappa_u X \\ B &= B_{\text{inst}} - A_b + Z_b + C_b(B - V) + \kappa_b X \\ V &= V_{\text{inst}} - A_v + Z_v + C_v(B - V) + \kappa_v X \end{aligned} \quad (6.7)$$

where:

U , B and V are the calibrated magnitudes in the three bands,

U_{inst} , B_{inst} and V_{inst} are the instrumental magnitudes in the three bands,

A_x is an arbitrary constant which is often added to the instrumental constants,

C_x is the colour-correction term,

Z_x is the photometric zero point between the standard and instrumental systems,

κ_x is the atmospheric extinction coefficient,

X is the air mass, and

subscripts $x = u, b, v$ refer to the individual bands.

The operational procedure is similar to that for calibration without a colour correction. For a set of observations of standard stars, Z_x , C_x and κ_x (where $x = u, b, v$) are unknowns which can be solved for by least squares fitting of equations 6.7. Once the coefficients have been determined, they can be used to compute the calibrated magnitudes of the programme objects. Higher-order terms may be introduced for more accuracy if needed. For example:

$$V = V_{\text{inst}} - A_v + Z_v + C_1(B - V) + \kappa_v X + C_2 X(B - V) + C_3 X^2(B - V) + \dots \quad (6.8)$$

The atmospheric-extinction coefficient may be variable and can include a colour term, e.g.

$$\kappa = \kappa' + \kappa''(\text{colour index}) \quad (6.9)$$

where κ' and κ'' are constants. Often κ'' is sufficiently small that κ can be assumed to be constant. If the colour term is significant then the straight line relation between the air mass and the apparent magnitude will appear curved. The following sections deal with the specific coefficients in more detail.

6.6 Atmospheric Extinction Coefficients

Atmospheric extinction is the dimming of starlight by the terrestrial atmosphere. The longer the path length the starlight travel through the atmosphere the more it is dimmed. Close to the horizon the star will be dimmed more than closer to the zenith. The observed brightness of a given star changes thus throughout the night.

The extinction coefficients can be determined using the same data set. This is accomplished by obtaining several observations of a pair of blue and red stars[38]. While for differential photometry a seasonal average is sufficient, for all-sky photometry the extinction must be determined at each observing run. *The pair of stars does not need to have previously determined UBV magnitudes. Only a large difference in instrumental colour is required.* This is very convenient, as any pair of stars will do, not necessarily only standards. Choose a pair of stars that will transverse a large range of air mass during the observing time available i.e., stars with a declination close to the celestial equator.

6.6.1 Second Order Coefficients

The second order coefficients are defined by k_v'' and k_{bv}'' in the following equations[38]. These coefficients correct for all the effects of extinction by airmass. The second-order extinction coefficients for each star of the red-blue pair are found by:

$$v_{o(red)} = v_{red} - (k_v' + k_v''(b-v)_{red})X_{red} \quad (6.10)$$

$$v_{o(blue)} = v_{blue} - (k_v' + k_v''(b-v)_{blue})X_{blue} \quad (6.11)$$

$$(b-v)_{o(red)} = (b-v)_{red} - (k_{bv}' + k_{bv}''(b-v)_{red})X_{red} \quad (6.12)$$

$$(b-v)_{o(blue)} = (b-v)_{blue} - (k_{bv}' + k_{bv}''(b-v)_{blue})X_{blue} \quad (6.13)$$

where

$v_{o(red)}$ = visual red star instrumental mag corrected for atmospheric effects

$(b-v)_{o(red)}$ = $(b-v)$ red star instrumental mag corrected for atmospheric effects

X_{red} = red star air mass at observation

$v_{red} = -2.5 \log_{10}(\text{averaged V filter red star reading})$

$b_{red} = -2.5 \log_{10}(\text{averaged B filter red star reading})$

$u_{red} = -2.5 \log_{10}(\text{averaged U filter red star reading})$

$v_{o(blue)}$ = visual blue star instrumental mag corrected for atmospheric effects

$(b-v)_{o(blue)}$ = $(b-v)$ blue star instrumental mag corrected for atmospheric effects

X_{blue} = blue star air mass at observation

$v_{blue} = -2.5 \log_{10}(\text{averaged V filter blue star reading})$

$b_{blue} = -2.5 \log_{10}(\text{averaged B filter blue star reading})$

$u_{blue} = -2.5 \log_{10}(\text{averaged U filter blue star reading})$

k_v' = first order visual extinction coefficient

k_{bv}' = first order $(b-v)$ extinction coefficient

k_v'' = second order visual extinction coefficient

k_{bv}'' = second order $(b-v)$ extinction coefficient

Subtracting 6.11 from 6.10 gives :

$$v_{o(red)} - v_{o(blue)} = (v_{red} - v_{blue}) - k_v'(X_{red} - X_v) - k_v''((b-v)_{red}X_{red} - (b-v)_{blue}X_{blue})$$

and similarly for 6.13 subtracted from 6.12 gives :

$$(b-v)_{o(red)} - (b-v)_{o(blue)} = ((b-v)_{red} - (b-v)_{blue}) - k_{bv}'(X_{red} - X_{blue}) - k_{bv}''((b-v)_{red}X_{red} - (b-v)_{blue}X_{blue})$$

Rewrite the equations as :

$$\delta v = v_{red} - v_{blue} \quad (6.14)$$

$$\delta v_o = v_{o(red)} - v_{o(blue)} \quad (6.15)$$

$$\delta(bv) = (b - v)_{red} - (b - v)_{blue} \quad (6.16)$$

$$\delta(bv)_o = (b - v)_{o(red)} - (b - v)_{o(blue)} \quad (6.17)$$

It can be assumed that $X_{red} \approx X_{blue}$ so that the mean air mass of the red-blue observation becomes just X . Then, the above equations become:

$$\delta v = k_v'' \delta(bv)X + \delta v_o \quad (6.18)$$

$$k_v'' = \frac{\delta v}{(\delta(bv)X + \delta v_o)} \quad (6.19)$$

$$\delta(bv) = k_{bv}'' \delta(bv)X + \delta(bv)_o \quad (6.20)$$

$$k_{bv}'' = \frac{\delta(bv)}{(\delta(bv)X + \delta(bv)_o)} \quad (6.21)$$

The slope of the graph of δv vs. $\delta(bv)X$ for several red/blue pairs gives k_v'' . A similar plot of $\delta(b - v)$ vs. $\delta(b - v)X$ gives k_{bv}'' .

6.6.2 First Order Coefficients

Having determined the k'' coefficients, the first-order coefficients can be solved. These are *independent* of the star's colour, and either the blue or red stars can be used, but not both at the same time. Using the blue star, the suitable equations are :

$$v_{blue} - k_v''(b - v)_{blue}X_{blue} = k_v'X_{blue} + v_{o(blue)} \quad (6.22)$$

$$k_v' = \frac{(v_{blue} - k_v''(b - v)_{blue}X_{blue} - v_{o(blue)})}{X_{blue}} \quad (6.23)$$

$$(b - v)_{blue} - k_{bv}''(b - v)_{blue}X_{blue} = k_{bv}'X_{blue} + (b - v)_{o(blue)} \quad (6.24)$$

Using several blue stars and plotting $(v_{blue} - k_v''(b - v)_{blue}X_{blue})$ vs. X_{blue} gives a slope with value k_v' . Similarly, a plot of $((b - v)_{blue} - k_{bv}''(b - v)_{blue}X_{blue})$ vs. X_{blue} has a slope k_{bv}' .

Although there are other techniques to calculate first-order coefficients, the method described here has the advantage that no other observations are needed except for those of the red-blue pair. Returning to the reduction of U filter data, we can write the relationship:

$$(u - b)_{blue} = k'ubX_{blue} + (u - b)_{o(blue)}$$

Then a plot of $(u - b)_{blue}$ vs. X_{blue} has the slope k'_{ub} . If the second-order extinction coefficients have temporal stability, they need not be re-determined on every night. Instead, a mean value for each k'' can be adopted while solving only for the first-order coefficients. This is best done by observing the rising (or setting) of a single star with an instrumental colour, $(b - v)$, close to zero and applying the last three equations in exactly the form as previously described.

The corrected magnitude for the star, after correcting for all atmospheric influences, can be calculated from

$$U - B = \phi(u_0 - b_0)(1 - k''_{ub}X) - \phi k'_{ub}X + \zeta_{ub} \quad (6.25)$$

$$B - V = \mu(b_0 - v_0)(1 - k''_{bv}X) - \mu k'_{bv}X + \zeta_{bv} \quad (6.26)$$

$$V = v_0 - k'_vX + \epsilon(B - V) + \zeta_v \quad (6.27)$$

$$B = (B - V) + V \quad (6.28)$$

$$U = (U - B) + B \quad (6.29)$$

Where

U, B, V = ultraviolet, blue and visual true magnitudes

ζ_x = zero points for each colour band

ϕ, μ, ϵ = ultraviolet, blue and visual colour transformation coefficients.

Alternative methods for first order coefficient

1. The absorption coefficient can be defined in terms of the ratio of the total incoming flux (f_i) to the observed flux (f_o) in the equation

$$K = 2.5 \log \frac{f_i}{f_o} \quad (6.30)$$

$$\text{and with } m_i = -2.5 \log(\text{counts/sec}) \quad (6.31)$$

$$K = \frac{\Delta m_i}{\Delta X}. \quad (6.32)$$

By observing different stars over a range in hour-angle, the slope of the graph of instrumental magnitude (m_i) vs. the airmass (X) gives the required value for the first order coefficient. This is known as Bouger's method.

2. Choosing a pair of standard stars close together in terms of time and hour-angle allows faster determination of K possible. This method is known as Hardie's method:

$$K = \frac{(m_{s1} - m_{s2}) - (m_{i1} - m_{i2})}{\Delta X} \quad (6.33)$$

where m_{sx} is the standard star known magnitude in a specific filter band and m_{ix} the instrumental magnitude of the standard.

Problems with the B filter

For filters V , R , and I , K are nearly the same for stars of all colours. This is not entirely true for high precision work. For the B filter, however, we have an additional complication, namely the extinction as a function of wavelength changes very rapidly over the B and U filter bandpass. This rapid change of extinction with wavelength over the bandpass causes stars of different colours to exhibit different amounts of extinction in the B filter. For very red stars, most of the light that comes through this filter is at the red end of the bandpass, where the extinction is lower than at the blue side of the bandpass. For blue stars, there is more light in the blue end of the bandpass, where the extinction is higher. Instead of the extinction coefficient being almost the same for all

colour of stars (as is the case for V , R , and I), K_B is a function of the star colour

$$K_B = K'_B + K''_B(B - V).$$

Here K'_B is the main extinction coefficient or the first order coefficient, while K''_B is the colour correction coefficient or the second order coefficient. As the extinction in B is less for a red star than for a blue star, K''_B must be a negative number.

To determine K''_B , observe a red- blue pair. These are two stars of very different colour that can be observed in the same CCD field. Measure, using preferably Bouguer's method (eq. 6.32), the B band extinction for the red star ($K_{B(red)}$) and for the blue star ($K_{B(blue)}$). These two numbers should be significantly different. We can use these two numbers then to solve for both K'_B and K''_B , using

$$K_{B(red)} = K'_B + K''_B(B - V)_{red} \quad (6.34)$$

$$K_{B(blue)} = K'_B + K''_B(B - V)_{blue} \quad (6.35)$$

Having $K_{B(red)}$ and $K_{B(blue)}$, together with the $(B - V)$ values for each star from the standard's catalog, solving for K'_B and K''_B is straightforward. The same reasoning also applies to the U filter.

6.6.3 Determining Colour Transformation Coefficients

Having determined the extinction coefficients that account for atmospheric effects, the next step is to transform the data to the standard UBVRI system. This is done by observing a set of standard stars with a wide range of known colors, applying the extinction corrections and then determining the coefficients using the following equations[38].

$$(V - v_0) = \epsilon(B - V) + \zeta_v \quad (6.36)$$

$$(B - V) - (b - v)_0 = \left(1 - \frac{1}{\mu}\right)(B - V) + \frac{\zeta_{bv}}{\mu} \quad (6.37)$$

$$(U - B) - (u - b)_0 = \left(1 - \frac{1}{\phi}\right)(U - B) + \frac{\zeta_{ub}}{\phi} \quad (6.38)$$

where

U, B, V = published standard's UBV magnitudes

u, b, v = observed magnitudes

ϕ, μ, ϵ = U, B, V colour coefficients

ζ_x = zeropoints

The slope of the graph $V - v_0$ vs. $(B - V)$ gives ϵ , and the y-intercept gives ζ_v . Similarly does one get $1 - 1/\mu$ and ζ_{bv}/μ from $(B - V) - (b - v)_0$ vs. $(B - V)$, and the values of $1 - 1/\phi$ and ζ_{ub}/ϕ comes from the graph of $(U - B) - (u - b)_0$ vs. $(U - B)$.

6.7 Standard Stars

Measuring the instrumental magnitude of a star and calibrating it against a set of standard stars for that specific band is the basis for effective so-called all-sky photometry. The instrumental magnitudes are thus converted to standard magnitudes that are reproducible. In this process standard stars for the system are re-observed and a comparison is done between the instrumental and standard or published magnitudes. If the instrumental system is a good match to the standard system then it may be possible to compare just the corresponding bands in the two systems. Conversely, if the two systems are less well-matched or high precision is required then the standard magnitude may have to be computed from the corresponding band in the instrumental system with corrections using the colour indices.

In order to be able to do successful photometry, standard stars should be selected that are similar to the intended observed object(s), with a colour range slightly wider than the colour of the observed object. This is however not always possible, as the standards are a selection of stars, with no equally spaced stars representing the whole of the photometric system. The standards should be observed throughout the observing run, with zenith angles approximating the observed object's. A plot of the observed magnitudes against computed air mass can be made with calibrated photometric measurements resulting.

Passing clouds and light mist will obviously affect the atmospheric extinction. Furthermore, they can be difficult to detect by eye. However, it is easy to spot any deterioration in the observing conditions if the atmospheric extinction is being monitored regularly. Observations of programme objects can be suspended until good atmospheric conditions prevail again. Optimal results are possible following this strategy. For this purpose the scripts developed during this study are extremely useful.

The rules for photometry are

- that programme objects should only be calibrated with observations of standards made on the same night,
- when standards are fitted the residuals should be examined individually and obviously outlying observations checked and/or discarded and
- the residuals should be checked for systematic trends.

6.7.1 Choosing Standard stars

The choice of standards is a critical one, as this becomes the basis for all further measurements. Although photometry can be handled as a straightforward process, it is not. As pointed out by Crawford [9], when doing photometry, a measurement is made including the effect of many things: the output from the astronomical body under study, any shells or discs surrounding it, interstellar matter, the effects from the Earth's atmosphere, the defects of the telescope and filters as well as the deficiencies of the detectors in use. Care must be taken when dealing with reddened stars, metal-poor or metal-rich stars, stars with composite spectra etc. [43] Standards used in the calibration process must thus bracket the characteristics of the system under study. Standards are done

with a specific set of filters, detectors and telescope. This system can never be exactly duplicated, due to the inaccuracies in manufacturing, allowed tolerances in specifications for filters and the position, height and humidity of the site. Other factors such as the transparency of the atmosphere and temperature will also add to the problems facing the calibration process.

There are several sets of standard stars that can be used. These standards were done with the Johnson UBVRI system or more appropriately for work at Boyden, the $UBV(RI)_C$ filter system. Standards most used are the Harvard E-region stars, which are centered around declination -45° . The magnitude range between $2 < V < 11.5$ and a colour range of $-0.2 < (B-V) < 1.6$. Most red stars in this set are gaints, with a few red dwarfs. The bluer stars are generally too bright for larger appertures [28].

The Harvard F-region stars are at declination -75° , evenly spaced in RA. In the fainter than 7.5 region, there is only one red star. Landoldt used the E-region and Johnson standards as reference to observe more than 250 stars with $V > 11$. These are centered around the equator.

Young [28] pointed out that to effectively measure extinction, one would need a standard star distributed every 30 minutes of arc, up to 2 airmasses on both sides of the zenith. This can not always be done with only a single catalogue, for instance the E-region standards, and care should be taken in selecting from different catalogues, as different colour measurements may be present.

6.8 Zero points

In the original magnitude system of Hipparchus, the stars were divided into six brightness classes. The brightest stars were put into the first class and the faintest into the sixth class. These sorting bins of brightness were called "magnitudes" which meant "size". There was no "Zero Point" in this original system. When photometry had developed to the point where brightness ratios of ten percent or less could be measured, the old system of brightness classes gave way to a continuous scale of brightnesses still loosely coupled to the old magnitude steps. Pogson suggested that a magnitude difference of one, represented a fixed ratio of flux. This is the ratio constant today. Two stars that have observed flux F_1 and F_2 will have a magnitude difference d_m defined by:

$$d_m = m_1 - m_2 = -2.50 \log \left(\frac{F_1}{F_2} \right) \quad (6.39)$$

$$m_1 = -2.50 \log \left(\frac{F_1}{F_2} \right) + m_2 \quad (6.40)$$

Equation 6.39 will allow an observer to accurately measure the magnitude difference between two stars. It will not give the magnitude of star 1 unless one first knows the magnitude of star 2 as shown in equation 6.40.

Equation 6.40 is used to give local magnitudes in preliminary reductions. F_1 and F_2 are measures of the flux in units of milliamperes on a current meter, volts on a voltmeter, mm of deflection on a chart recorder, photon counts from a pulse amplifier, or ADUs from a CCD apperture photometry reduction program. By way of an example : if one assumes that F_2 has a value of 1.000, and m_2

has a value of 0.000, then :

$$m_1 = -2.50 \log(F_1).$$

The values of m_1 are on a local magnitude scale. One can calculate magnitude differences from the local system that would compare with those differences measured by others. If observer A uses photon counts and observer B uses ADUs, their local magnitudes will be quite different but their magnitude differences would be the same, excluding extinction corrections or filter transformations. Local magnitudes can be converted into standard magnitudes by the addition of a zero point. The zero point is a function of the units used to measure flux, amplification factor of the instrument, size of the telescope, atmospheric extinction, and other factors influencing the measurement with a specific device and filter set. For example, the V magnitude of Sirius is given as -1.45 while Alcor is 4.03. The magnitude difference is thus 5.48 . One could define Sirius to be 1.00 which would make Alcor 6.48 . The magnitude difference is the same in either case. Only the zero point has been shifted.

When Johnson and Morgan produced their photoelectric catalog in 1953, they were measuring to two decimal places. They had to assign a zero point to their photometric system that would make it similar to previous systems. The V magnitudes assigned to their primary standards were chosen so as to match the International System then in use. The Johnson V magnitudes differ from the Harvard visual photometry system by about 0.1 magnitude. The Harvard photometry system has been the basis of the visual magnitudes on the AAVSO charts. Comparison star extrapolations to fainter magnitudes introduced large systematic errors which plague older charts to this day. CCD chips have a large dynamic range and can extend sequences to fainter limits with better accuracy than by earlier methods. For this reason the V magnitudes of Johnson are chosen as defining the zero point of the visual magnitude system for future charts.

6.9 Determining the night's photometric quality

To do accurate photometry, it is necessary to know what the sky is doing throughout the observations. A suitable sequence of stars that will suit this purpose will be a set of stars that span the magnitude range of the variable, and also bracket the variable's colour. They would be used to set the zero point for the magnitudes in a given field, and optionally can be used as comparison stars for the variable. Sequences that would be used for determining the transformation coefficients for a given CCD and filter set are best when the stars have the same magnitude but span a wide range in colour. All sky photometry, using the Landolt standards, is performed by determining the nightly instrumental zero point, transformation coefficients and atmospheric extinction coefficients and the use of these parameters to adjust the instrumental photometry so that standardized magnitudes can be predicted.

To determine the various parameters, care should be taken to have a wide range of colours, as well as good flat fields, so that no gradient is present in the fields that must be measured. Different techniques are needed e.g. to take a sequence of objects on the celestial equator and an object at a high opposite sky-latitude to that of the observatory. In obtaining the sequences, only nights that are photometric should be used, i.e clear with no clouds, dust, smog or smoke and with seeing reasonably good and stable. Standard fields where many standards fall within the field of view of

the CCD are preferred. An example is SA110-503 where 8 Landolt standards are within a 5 arcmin radius. The end result is a schedule of observations, where the program fields are interspersed with standard star observations.

For a telescope the size of the 1.5-m Boyden telescope, any star brighter than about magnitude 10 is too bright, and a test exposure should indicate the suitable exposure time. The final exposure should be such that the brightest star does not saturate the detector and the faintest star still has enough signal-to-noise to provide a good measure. For most CCDs, this dynamic range is between 4 and 5 magnitudes. A field that contains a magnitude 11 star will give reasonable photometry down to magnitude 16 or so in a single exposure. More dynamic range than this can be obtained by taking at least two frames with differing exposure times. In that case care should be taken to adjust the exposure times so that there is at least a magnitude overlap between exposures. Because of the linearity of the CCD, this resulting magnitude range is likely to be very close to the truth.

This of course should be done in at least two filters, so that a colour can be obtained that can be used in the transformation process. If only a V filter is used for example, a red star in the frame would be systematically brighter or fainter than a blue star. The frames with differing filters will most likely have to have different exposure times as well. Landolt used an aperture of 10–14 arcsec, so using the same size while doing aperture photometry would include the same faint stars that he included in his original work.

After the normal transformation and extinction calculations the results can be compared with the published values. The standard deviation of these measures gives a measure of the stability the night and how well any star's magnitude can be estimated. The error for a given star is given by

$$E_{star} = \sqrt{\sum \sigma^2 + E_{p(x)}^2}$$

i.e. the square root of the sum of the nightly standard deviation squared plus the Poisson error squared of the star in question. A good photometric night should have a standard error of less than 0.02 magnitudes.

Systematic effects in a single night's observation of a program field can skew the results. The only way to get a good handle on these errors is to measure each field on at least two, and preferably three or more, nights and compare the results. This is of course only practical with an observing program spanning several weeks. By measuring on different nights, a check can be done for variability of stars within the field, especially if the nights in question are spaced several nights apart. By taking the average of the measures, a better determination of the field magnitudes can be obtained, and by taking the standard deviation of the measures of a given object, a better understanding of the real errors in the measurement of that object can be determined. Really good results can be obtained when the standards are selected to cover the whole sky, and ideally if a standard star appeared in every frame taken with the CCD, but that is not currently the case. The rule of thumb should be to always take at least two measures of a field, and use a single measure of a field only as a last resort.

After calculating the mean magnitude and standard deviation for each object measured, a scatter plot of magnitude vs. error gives a measure of the data quality. This plot will show the typical ridge line of Poisson photometric error. This kind of plot finds poor nights quickly if there are three or more nights represented in the plot, since the smallest error, that is for the bright stars, will be increased and the plot will look like there is an added offset. If the night was really non-photometric, an offset of a tenth of a magnitude or more for the well-exposed stars will be seen.

If a photometric sequence is needed quickly, for example when weather changes are expected, the program field can be bracketed by standard fields on either side, either in time or in space. This can yield reasonable results in a short period of time.

6.10 Accuracies

There will always be some error associated with CCD measurements. Poissonian statistics determines that the accuracy with which a measurements of incoming photons can be made varies as the inverse square root of the number of photons recorded. For example, 10^6 , photons has a square root of 10^3 and so the accuracy of that measurement is 10^{-3} which is 0.001 magnitude. The less counts, the less accuracy can be obtained. The ability of the CCD to record and read out counts in each pixel is known as 'the full well capacity'. A CCD with 9 micron pixels has a full well capacity of about 70 000. A scientific quality CCD with 25 micron size pixels has a full well capacity of around 400 000. The best possible accuracy from the first is about $1/\sqrt{400000} \approx 0.004$ magnitudes and from the latter about 0.002 magnitudes.

The same reasoning applies to the measurement of noise. There are of course many contributing factors to the noise, but consider the random noise contribution of counting photons. When counting photons with an aperture, the aperture count would include signal from the sky and star, thus the "noise" count is given by $\sqrt{C_{sky+star}}$, with the noise in the sky section $\sqrt{C_{sky}}$. The total noise contribution can be written as[38]

$$N = \sqrt{C_{star} + 2C_{sky}}$$

so that the general equation of the signal to noise ratio is given by

$$S/N = \frac{C_{star}}{\sqrt{C_{star} + 2C_{sky}}}. \quad (6.41)$$

With large values for the star counts, the sky contribution becomes small, so that $S/N \propto \sqrt{C_{star}}$, but for small values of the star counts, the sky's contribution can dominate and $S/N \propto \sqrt{2C_{sky}}$. This means that at a certain point, the sky will dominate and the star will be "lost" in the brightness of the sky (fig. 6.2).

Another source of error is the scaling down of say 400 000 counts to a 16-bit AD converter full scale reading of 65 536 counts. Each of the values has been divided by 8 to obtain this number. Low counts around 1, 2 etc. will be scaled to 8, 16, etc. This does not seem to be problematic, but for low pixel values, a reading of around 20 will be scaled to either 16 or 24, with an associated error

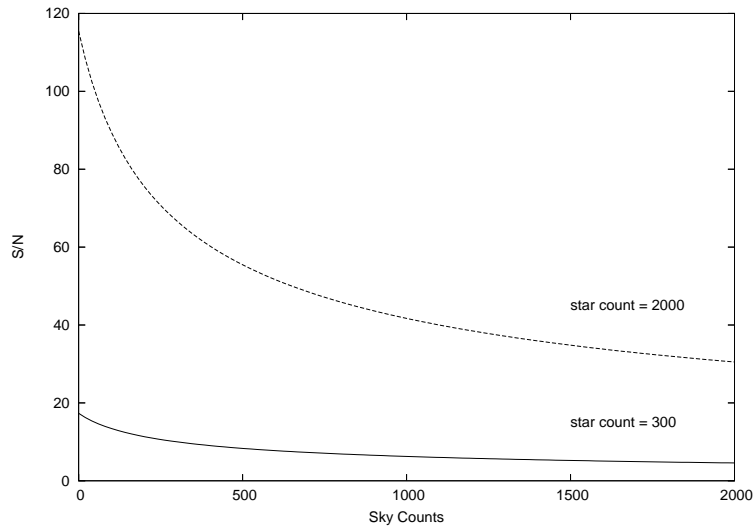


Figure 6.2: Calculated signal to noise ratio of a bright star (star count=2000) compared to a dim star (star count =200) plotted against the sky count

of eight. Subtracted from a very bright star around saturation point, the potential accuracy can be between $1/265$ to $1/632$. But with very dim stars on the same chip, say five to ten magnitudes below the saturation level of the chip, counts as low as 4 000 to 200 can be read. That is a potential accuracy of $1/63$ to $1/20$, so an accuracy of at best 0.2 is then possible for really dim stars. Using separate exposures for bright and dim objects on the same image could be used to overcome this problem.

Other potential problems can be the way that the shutter works. A leaf shutter opening to a side can cause a variation in exposure over the chip, as one section of the chip will be illuminated a fraction of a second longer than the side exposed last. This is a problem in extreme short exposures. As flats are normally taken over longer time spans, it will not reflect this uneven illumination. Using shorter exposures when taking flats can be helpful in this case.

The other source of error is the cloudiness of the sky. Traditional, single channel, photoelectric photometry is just about impossible unless sky conditions are good. Transparency variations due to passing clouds, even clouds so faint that they cannot be seen with the naked eye, can often be tens of percent. The assumption that transparency variations due to clouds will average out over the field of view because the fields of view are small and the images are all obtained simultaneously is wrong. If the exposure is several minutes duration and the clouds are moving rapidly then this assumption might be valid. However, if the clouds are slow moving, sharp edged cumulus, alto cumulus or similar, and if the exposure time is short then the assumption might not be valid. If you are using a large area CCD with a short focal length system so that the field of view is large then even more care has to be taken with this potential source of error. If the project requires high accuracy photometry and if there is any doubt about the quality of the sky, several exposures must be made. Continual monitoring of the magnitudes on each frame must be done and the mean and standard error from all the measurements evaluated. The standard error thus obtained gives a valid measure of the accuracy of the results. Scintillation is another source of error and is governed by the size of the telescope.

Chapter 7

A Pipeline for Photometric Measurements

7.1 Reduction and Photometry Pipeline

A schematic of the outline of the photometry scripts are shown in figure 7.1.

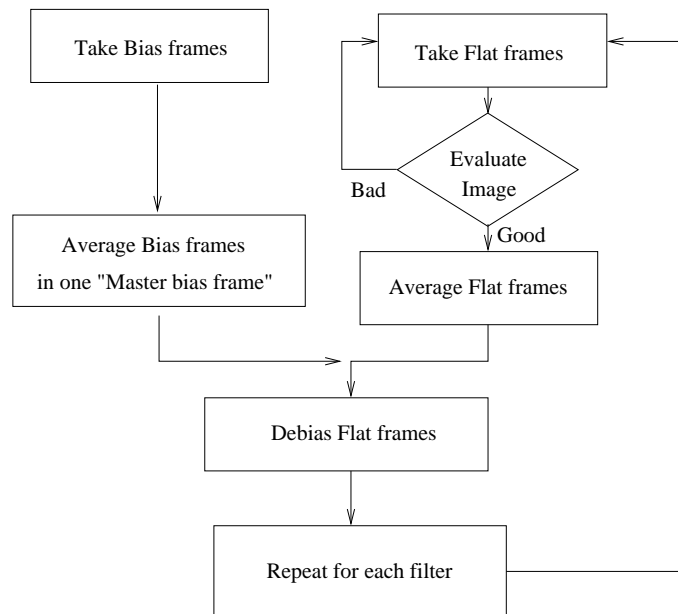


Figure 7.1: Schematic outline of the photometry scripts

The full photometry process can be outlined as follows:

1. Take bias and flats images
2. Reduce bias and flats, i.e.
 - average bias images into on *master bias* image
 - subtract the master bias image from each flat image
 - average, for each filter, the flat images and create a filter master flat image

3. Observe star and standards in all filters needed. Standards must have a range of colours and a bigger range in hour angle than the observed star(s).
4. Reduce data by subtracting averaged master bias and divide with appropriate filter flat
5. Correct for atmospheric effects.
6. Measure instrumental magnitudes.
7. Transform instrumental magnitudes to standard magnitudes.
8. Determine uncertainty.

7.1.1 CCD reduction

A selective collection from the Starlink packages is used to manage the photometry. Although most of the Starlink distribution is available on MENSA and PAVO, only the appropriate photometry programs used will be described here. The process of CCD reduction is fully described in section 5.3. The outline for the CCD reduction process is:

1. Take and evaluate bias and flat images
2. Make and evaluate a master bias frame of all bias frames averaged.
3. Make and evaluate a master flat frame for each filter of all frames for a specific filter averaged.
4. Debias the master flats with the master bias frame created.
5. Debias the target frames (object/project stars) with the master bias frame.
6. Debias the target frames in a specific filter band with the master flat for that filter.
7. Evaluate results

This process should produce cleaned data reduced of all contamination and instrumental effects, usable in photometry.

7.1.2 Photometry Measurements

Photometry is mainly done through the use of the KAPPA kernel package and PHOTOM in the Starlink Software collection. For the photometry as done in this system, all data files are expected to be in the FITS format. In order to make the procedure as painless as possible for users of the data pipeline, extensive use of scripts in the tc-shell under Linux are used to automate most of the tasks done by the observer in obtaining photometry results. *No attempt is made to fully automate the whole process, as human judgement is frequently needed throughout the whole process of data reduction and obtaining accurate photometry results.* The idea is not to produce a total "black box" approach.

The reasoning behind the development of the scripts is to provide an semi-interactive means of processing lots of data fairly quickly. These scripts are not considered to be generic and applicable to all observing programmes, but if the observing programme is followed as outlined in the telescope manual, then the scripts will make handling and getting the data afterwards, easier. The

scripts underwent several changes and updates, and what is described here, is the content of the scripts at the time this thesis is written.

The biggest change to the scripts occurred during 2004, when the department joined the PLANET collaboration. The scripts used by the PLANET collaboration required the filenames to be in a different format than that adopted for use at the observatory. At first it was decided to add scripts to post-process the FITS files, so that the final format of the files would be compatible with the PLANET scripts, but to have an universal setup, the scripts were rewritten to accomodate the processing of a sequence of data, spanning months and even seasons.

The reduction is handled by a few scripts, namely **Makebias**, **Makeflats** and **Makeimages**. These scripts were written to reduce all the files present on BOOTES. These files will be written to the directory `/data/ccd/image` on the host machine and left in the NDF format for use with STARLINK software. PLANET data will be changed to FITS files and copied to the PLANET directories, to be measured by the PLANET pipeline. Full details are available in the telescope and observing manual. Photometry are handled by two scripts measuring the instrumental magnitudes of the program stars (**datamag**) and the standards (**stmag**). The purpose of each script is described below.

Makebias and Makeflats

These two scripts are basically the same. They check the hard-linked directory `/bootes` for any new bias and flat files not reduced and reduce the bias files and use the correlating bias frame for the specific date to reduce the flat field image. These files are stored with the date as prefix to the filename.

Makeimages

This script expects three parameters, namely the project, object and date of the observations. This enables the script to be used interactively while taking data as well as repeating previous reduction runs. The script proceeds to reduce the data of the object, over all the observation dates present if a date is not specified. Logs are kept in `/data/ccd/logs/object.log` to prevent duplicate processing of files. This file can be edited to reprocess images, although previously processed images will still be on disc. It is assumed that the user will have a good knowledge of exactly what he/she is doing. It is expected that an additional script will see the light that will make life easier for the observer.

RealTime

During observations, reduction of files should be done as soon as data is saved. This can be done using the RealTime script. This script set the date to the current night's date and check the hard linked directory `/bootes` for any file that was observed during the night. It proceeds by passing the project and object name of this file with the date to the **Makeimages** script. Ideally this script should be run in a terminal window of its own, since it produces a lot of feedback on its progress for the observer.

stmag

This script assumes the data is reduced already. Prompts the user for the standard star to do photometry on. This script will either use colour data available in `/pub/standards` or it will proceed by asking for the appropriate information on the colour values. The interactive measurements of the magnitudes will be done. A position file, that was created with *SPICA*, can be used if present. The output of the script is a file containing all the photometric data needed to calibrate the system.

datamag

Basically duplicates what was done in *stmag*, with the exception of the colour data and the different layout of the resulting data file produced. A separate file containing magnitudes useful for comparing stars differentially is also created if more than one star on the image is measured.

7.1.3 Determining reduction coefficients

The reduction coefficients is a manual process, where the observer has to do all the work. The program of choice for linear regression during the development work was *gnuplot*. It is freely available under Linux as well as Windows environments and very easy to implement. It has the possibility to do weighted linear regression which sometimes produced the best results.

7.1.4 Aperture and optimal photometry

In order to do semi-automated photometry, certain general decisions had to be made. The software used (KAPPA) can be used in either optimal or aperture mode. Once applied to data, the choice became critical as magnitude differences of up to two magnitudes resulted during several test runs. Using test frames with sparse and dense star images, instrumental magnitude estimates were made with aperture and optimal methods, using different size circular apertures for aperture and optimal measurements. The results are shown in figure 7.3 and 7.4. From these results it is clear that aperture measurements is not a good choice. In dense star fields aperture measurements are not possible, as expected. The results are comparable to the theoretical curves, see figure 6.2. Care should however also be taken when using optimal photometry, as the seeing will determine the optimal aperture size to use.

7.1.5 Colour coefficient determination

The photometric coefficients of an extensive observing run on standards were determined (table 7.1). The results obtained are summarised below.

The instrumental magnitudes are determined by

$$m_\lambda = -2.5 \log C_\lambda$$

with C_λ the instrumental signal count for an exposure count of 1 second. The corrected instrumental magnitudes for an airmass(X) of zero, is given by

$$(m_\lambda)_0 = m_\lambda - k_\lambda X$$

where

$$k_U = 0.491$$

$$k_B = 0.280$$

$$k_V = 0.181$$

$$k_R = 0.125$$

$$k_I = 0.091.$$

To transform the measured values to the UBVRI system, we have the equations

$$U = (m_U)_0 + 0.153(U - B) + 20.166$$

$$B = (m_B)_0 + 0.073(B - V) + 22.216$$

$$V = (m_V)_0 - 0.064(B - V) + 22.375$$

$$R = (m_R)_0 + 22.501$$

$$I = (m_I)_0 + 0.130(R - I) + 22.357$$

and finally in terms of measured magnitudes

$$U = 1.147(m_U)_0 - 0.147(m_B)_0 + 19.870$$

$$B = 1.083(m_B)_0 - 0.083(m_V)_0 + 22.204$$

$$V = 1.074(m_V)_0 - 0.074(m_B)_0 + 22.387$$

$$R = (m_R)_0 + 22.501$$

$$I = 0.879(m_I)_0 + 0.121(m_R)_0 + 22.372.$$

7.2 Verifying photometric measurement accuracy

To verify the photometry routines, two test runs are presented. In the first run, a choice of only 6 standard stars were made on a night when the seeing stayed fairly constant. The details of the chosen stars are tabulated in table 7.2. The Landolt standards 110-229, E6-73, E7-97 and Wolf 629 were used for the linear fit of the difference of the catalogue and instrumental magnitudes against the atmospheric extinction. The result of this fit is shown in figure 7.5. The problems that was encountered with the bias frames and flatfields, as described earlier, were carefully controlled by taking a lot of twilight as well as midnight flats centred on empty starfields, with the telescope moved between images, as to eliminate any star images that may be present. The flats obtained were analysed for any gradient effects and any frame displaying gradient or periodic noise signa-

tures were discarded. This produced a useful set of reduced flats to work with and the results obtained were satisfactory. Dome flats were not feasible, as the dome is made of wooden struts closely spaced, casting distinct structure in the flats. No part of the dome produced evenly illuminated flats, and a test run, where the telescope was moved slightly between images, so that the structure "panned" the field of view, did not produce good results.

7.2.1 Scientific publications submitted that used Boyden data

The software developed consists of two three parts, namely

- the camera control software,
- the image reduction pipeline,
- and the photometry pipeline.

The papers published with Boyden data, relied on the camera control software and the data reduction pipeline. Below is a list of publications that have appeared so far utilising these two components. As Boyden joined the PLANET collaboration only a year before this thesis was written, it should be noted that there are a few publications still in progress that are also making use of Boyden data. Details can be found on the PLANET home page <http://planet.iap.fr>.

1. Abe, D.P. *et. al.* 2003, A&A, 411, L493
Probing the atmosphere of a solar-like star by galactic microlensing at high magnification
2. Bersier, D.*et. al.* 2003, ApJ, 584, L43-L46
The unusual optical afterglow of the gamma-ray burst GRB 021004: Color changes and short-time-scale variability
3. Yock, P. *et. al.* 2003 IAUS 219E
Precision Measurement of Limb Darkening by Microlensing
4. Bennett, D.*et. al.* 2002 ApJ 579
Gravitational Microlensing Events Due to Stellar-Mass Black Holes
5. Rhie, S. *et. al.* 2000 IAUS 202E
Microlensing Planet Search Project

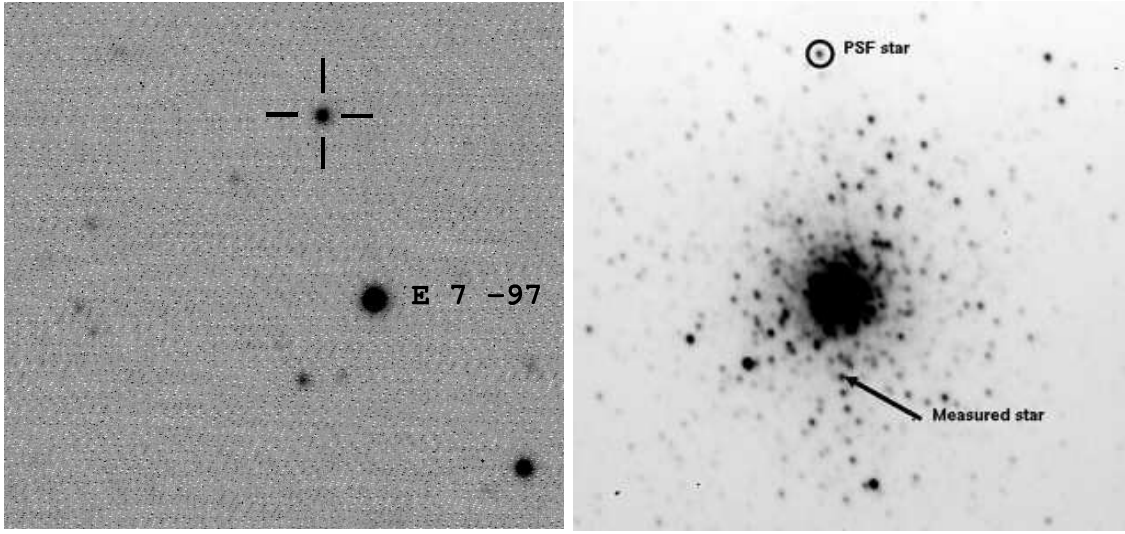
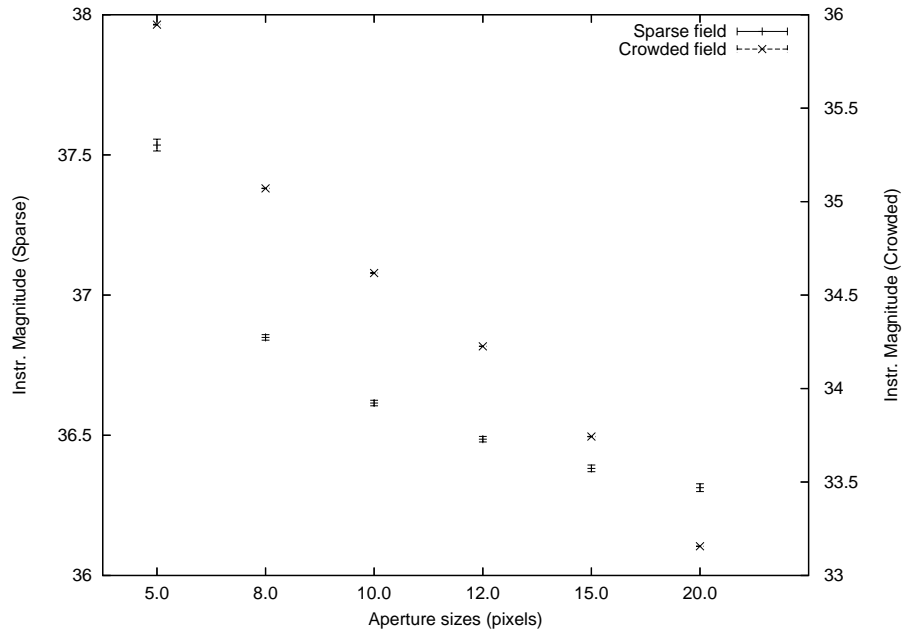
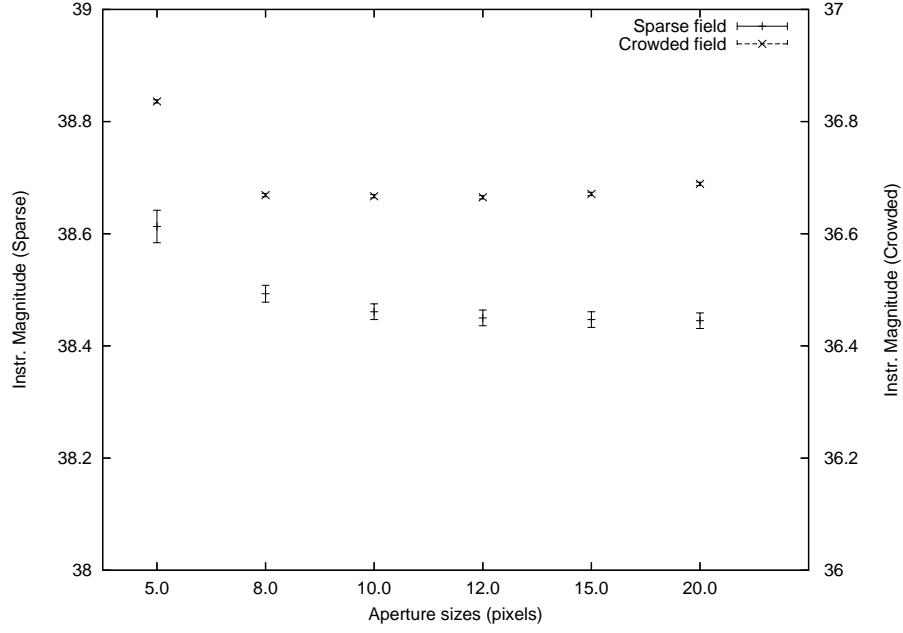


Figure 7.2: Fields of E7-97 showing the single star and crowded field M54 with the PSF-star and measured star used for optimal aperture testing shown.



| | E7-97 : Non-crowded field | | | M54 : Crowded field | | |
|----------|---------------------------|-------|--------|---------------------|-------|---------|
| Aperture | Inst. mag. | Error | Counts | Inst. mag. | Error | Counts |
| 5.0 | 37.535 | 0.021 | 96862 | 35.947 | 0.002 | 417959 |
| 8.0 | 36.849 | 0.010 | 182099 | 35.071 | 0.001 | 936766 |
| 10.0 | 36.615 | 0.010 | 226011 | 34.618 | 0.001 | 1421000 |
| 12.0 | 36.486 | 0.010 | 254360 | 34.226 | 0.001 | 2039000 |
| 15.0 | 36.382 | 0.012 | 280154 | 33.743 | 0.001 | 3181000 |
| 20.0 | 36.313 | 0.014 | 298498 | 33.156 | 0.000 | 5466000 |

Figure 7.3: Aperture photometry - Measured instrumental magnitudes for fields in figure 7.2.



| | E7-97 : Non-crowded field | | | M54 : Crowded field | | |
|----------|---------------------------|-------|--------|---------------------|-------|--------|
| Aperture | Inst. mag. | Error | Counts | Inst. mag. | Error | Counts |
| 5.0 | 38.613 | 0.029 | 35861 | 36.836 | 0.003 | 184412 |
| 8.0 | 38.493 | 0.015 | 40072 | 36.669 | 0.003 | 214964 |
| 10.0 | 38.461 | 0.014 | 41252 | 36.667 | 0.003 | 215436 |
| 12.0 | 38.450 | 0.014 | 41671 | 36.665 | 0.003 | 215833 |
| 15.0 | 38.447 | 0.014 | 41815 | 36.671 | 0.003 | 214517 |
| 20.0 | 38.445 | 0.014 | 41881 | 36.689 | 0.003 | 210972 |

Figure 7.4: Measured instrumental magnitudes for indicated stars in figure 7.2 using optimal photometry.

| Star | V | B-V | U-B | V-R _c | V-I _c |
|--------|--------|--------|--------|------------------|------------------|
| E1 05 | 9.451 | 0.365 | -0.038 | 0.225 | 0.453 |
| E1 76 | 8.945 | 1.302 | 1.140 | 0.680 | 1.302 |
| E1 16 | 9.756 | 0.596 | 0.111 | 0.333 | 0.641 |
| E1 35 | 9.464 | 1.428 | 1.710 | 0.770 | 1.506 |
| E1 20 | 9.852 | 0.745 | 0.282 | 0.408 | 0.781 |
| E1 75 | 9.706 | 0.247 | 0.083 | 0.140 | 0.277 |
| E2 238 | 9.667 | 1.436 | 1.760 | 0.759 | 1.422 |
| E2 56 | 9.900 | 0.963 | 0.763 | 0.533 | 0.993 |
| E2 55 | 10.312 | 0.470 | 0.010 | 0.268 | 0.259 |
| E2 03 | 9.666 | 0.251 | 0.073 | 0.150 | 0.308 |
| E3 72 | 10.754 | 0.351 | 1.241 | 0.854 | 1.635 |
| E3 83 | 10.010 | 0.305 | 0.044 | 0.195 | 0.388 |
| E3 09 | 8.912 | -0.041 | -0.256 | -0.020 | -0.044 |
| E3 75 | 9.926 | 0.791 | 0.359 | 0.437 | 0.840 |
| E3 65 | 9.622 | 1.147 | 1.102 | 0.580 | 1.098 |
| E3 54 | 10.150 | 0.114 | -0.017 | 0.082 | 0.187 |
| E3 30 | 8.996 | 0.568 | 0.012 | 0.316 | 0.637 |
| E3 96 | 9.934 | 1.486 | 1.738 | 0.802 | 1.523 |
| E3 12 | 9.664 | 0.151 | 0.099 | 0.094 | 0.201 |
| E4 24 | 8.505 | 0.489 | -0.017 | 0.282 | 0.568 |
| E4 108 | 9.772 | 1.890 | 2.130 | 1.013 | 1.948 |
| E4 17 | 9.602 | 0.200 | 0.164 | 0.136 | 0.265 |
| E4 26 | 10.003 | 0.549 | 0.033 | 0.314 | 0.615 |

Table 7.1: List of standard stars used for determining the first order, second order and transformation coefficients of the Boyden filters.

| E7-52 | Catalogue Magnitude = 10.776 |
|--------------------|------------------------------|
| Measured Magnitude | Difference |
| 10.697 | 0.079 |
| 10.711 | 0.065 |
| 10.712 | 0.064 |
| 10.709 | 0.067 |
| 10.711 | 0.065 |
| E7-62 | Catalogue Magnitude = 10.924 |
| Measured Magnitude | Difference |
| 10.957 | -0.033 |
| 10.925 | -0.001 |
| 10.927 | -0.003 |
| 10.920 | 0.005 |

Table 7.2: Photometric comparison of E7-52 and E7-62 as "unknowns" to evaluate photometry procedures

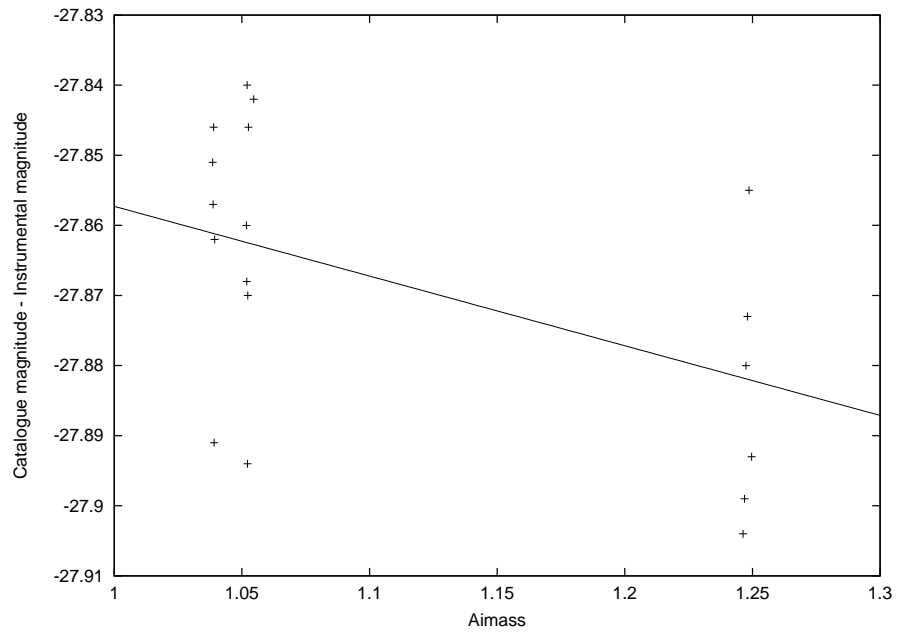


Figure 7.5: Fit of catalogue and instrumental magnitudes against atmospheric extinction for Landolt standards 110-229, E6-73, E7-97 and Wolf 629

Chapter 8

Conclusion

8.1 Image capturing software

The developed software, SPICA, is a camera control program, responsible for the image capture, display and storing of the images in FITS format. This program performed extremely well, and is in constant use at Boyden Observatory at the time of writing. The program is easy to use for short integration times and files can be saved in rapid succession, enabling more data coverage of critical events, i.e. microlens magnification events. This ability was well illustrated in the observations of MOA 2002-BLG33 and 2002-BLG42 as extrasolar solar system candidates.

Another feature of SPICA is the ability to sweep pre-determined error boxes. Before the installation of an internet connection at the observatory, searching for GRB afterglows was a bit like "shooting in the dark". Coverage of the error box was mostly done without a proper finding chart. After the internet installation, the errorbox facility allows a quick way to locate the dim afterglow, if any. Two extraordinary GRB afterglows were detected though, namely GRB021004 (Bersier, *D.et. al.* 2003, ApJ, 584, L43-L46) and GRB021010, the brightest GRB so far detected.

8.2 Reduction and photometry pipeline

The reduction pipeline started out, before the internet installation, in a format suitable for in-house data reduction. The reduced images for the MACHO and GRB afterglow collaborations were put on CD ROM and transferred to a FTP server at the University of the Free State. This was not ideal at all, as the data was usually transferred after the observer went to bed. The principal investigator in the collaboration was not able to interact with the observer except via telephone communication. The installation of an internet connection changed the way work was done and results were evaluated and instructions to the observer were easier to convey.

As the microlens collaboration changed from the MACHO to the PLANET group, the data pipeline had to be rewritten to accommodate the PLANET pipeline used to evaluate the images in real time. The images needed to be in a FITS file format for the PLANET pipeline, while the STARLINK routines used a NDF format. A differentiation as to the end product of the reduction pipeline was needed. PLANET related images are stored as FITS files for processing in the PLANET pipeline

with a specified filename structure. All other files are stored as NDF files ready for photometry with STARLINK software.

8.3 Problems and solutions

- The stuck shutter caused flatfields with gradients. The solution was to take midnight flats combined with some of the twilight flats, but images had to be evaluated before use.
- The primary mirror baffle problem was solved by inserting a baffle consisting of four rings as shown in figure 4.6.
- The electronic noise introduced by the analogue-to-digital converter card in the camera controller could not be fixed. The decision was made to buy a new camera from a reputable company, probably Apogee, but a final decision had not been taken at the time of writing. The CCD chip in the Pixelvision camera head is working perfectly, and a future scenario may see the camera head connected to a good camera controller again.
- Broken primary cell supports were fixed. These broken supports caused a shifting slanted star image when going through the focus.
- The personnel at Boyden received training in the removing and replacing of the main mirror, the adjustment of the mirror cell and collimation.

8.4 Suggestions

Primary baffle The rings of the baffle may be increased to five or six, and the baffle may be extended as well, but so far, a huge improvement is noticed in the image quality.

Secondary baffle The secondary baffle is too big. It obscures an unnecessary large part of the primary mirror. A smaller baffle can be used.

Stray light To prevent stray light from entering the CCD, a covering for the top part of the telescope has been suggested.

Dome seeing To improve dome seeing, the existing windows in the dome can be replaced by aluminium shutters that should be opened before the start of an observing session. Not only will excess light and heat during daytime be eliminated, but stray light from light pollution will be minimised. The standard procedure should be to open the dome at sunset, pointing away from the Sun.

Telescope seeing Airflow over the primary mirror is needed to combat the effects of turbulence in the closed bottom part of the telescope.

Camera The camera should be bought from a reputable supplier. A back illuminated chip with a good quantum efficiency and big pixel size ($\sim 24\mu\text{m}$) is needed.

Software Added controls for the filter wheel and focus motors need to be incorporated into SPICA.

Autoguider A database of suitable guidestars with coordinates is needed to make proper use of the autoguider.

Gears Frequent cleaning of the gears is required to combat the problem of dust entering the gears which increases the effect of the periodic error, trailing images and limit exposure times to less than four minutes. A lot of observing time is lost during studies of dim objects. Alternatively, a dust cover for the gears should be installed.

The usability of the telescope was improved by the developed software to a point where full coverage of rapid changes in the object under study is possible. This makes the telescope suitable for studies of microlensing events as well as the erratic emissions of accretion driven systems. The 1.5-m size of the telescope also enables the detection of GRB afterglows, and after the work done on the optical alignment and baffles, a fruitful observing season is in the pipeline for the 1.5-m Boyden telescope!

Bibliography

- [1] Abe F. *et. al.*, 2003, *Astronomy and Astrophysics*, 411, L493-L496
- [2] Alcock C., *et al.*, 1996, *Astrophysical Journal* 461, 84.
- [3] Allen C.W., 1973, *Astrophysical Quantities*, 3rd. ed., Athlone Press, London
- [4] Aly J.J., Kuijpers J., 1990, *Astronomy and Astrophysics*, 227, 473-482
- [5] Andrews A.D., *Irish Astronomical Journal* 25(2), 129-166 (1998)
- [6] Bennett D.P., Rhie S.H., 1996, *Astronomical Journal* 472, 660-664
- [7] Bessell M.S., *Precision Photometry*, pp. 46-56, SAAO, 2-3 February 1993, Kilkenny D., Lastovica E., Menzies J.W. (eds.)
- [8] Blandford R.D., Znajek R.L., 1977, *Monthly Notices of the Royal Astronomical Society*, 179, 433
- [9] Crawford D.L., *Precision Photometry*, pp. 18-24, SAAO, 2-3 February 1993, Kilkenny D., Lastovica E., Menzies J.W. (eds.)
- [10] Currie M.J., 1998, SC/4.2 C-shell Cookbook, Starlink Project, Rutherford Appleton Laboratory
- [11] Currie M.J., Berry D. S., 2000, SUN/95.16 KAPPA — Kernel Application Package Starlink Project, Rutherford Appleton Laboratory
- [12] Davenhall A.C., Privett G.J., Taylor M.B., June 1999, SC/5.2 The 2-D CCD Data Reduction Cookbook, Starlink Project, Rutherford Appleton Laboratory
- [13] Draper P.W., SUN/139.9, 1998, CCDPACK—CCD Data Reduction Package, Starlink Project, Rutherford Appleton Laboratory
- [14] Eaton N., Draper P.W., Allan A., 1999, SUN/45.10 PHOTOM — An Aperture Photometry Package, Starlink Project, Rutherford Appleton Laboratory
- [15] Eaton N., Privett G.J., 1996, SUN/42.5 DAOPHOT — Stellar Photometry Package, Starlink Project, Rutherford Appleton Laboratory
- [16] Howell S.B.(ed), 1992, *Astronomical CCD Observing and Reduction Techniques*, *Astronomical Society of the Pacific Conference Series*, 23
- [17] Kitchin C.R., 1998, *Astrophysical Techniques*, 3rd. ed., Inst. of Physics

- [18] Landolt A.U., 1992, *Astronomical Journal*, 104, 340-371.
- [19] Melsheimer F., www.fdm.com/boyden.html
- [20] Frank J., King A.R., Raine D.J., 1992, *Accretion Power in Astrophysics*, 2nd ed. Cambridge University Press
- [21] Gould, A., Welch, D., 1996, *Astrophysical Journal*, 464, 212
- [22] Hardie R.H., 1962, Ch. 8, *Astronomical Techniques*, Hiltner W.A. (ed.)
- [23] Harwitt, M., 1973, *Astrophysical Concepts*, John Willey & Sons.
- [24] Jarret A.H., 1981, Occational Publications no.2, Boyden Observatory
- [25] Joss P.C., Rappaport S., 1984 *Annual Review of Astronomy and Astrophysics*, 22:537-592
- [26] Lang K.R., 1999, *Astrophysical Formulae*, Volume II, Springer Verlag
- [27] Meintjes P.J., 2002, *African Skies*, 7:5-8
- [28] Menzies J.W., *Precision Photometry*, pp. 87-93, SAAO, 2-3 February 1993, Kilkenny D., Lastovica E., Menzies J.W. (eds.)
- [29] Mészáros P., astro-ph/9904038
- [30] Mészáros P., Rees M.J., 1997, *Astrophysical Journal* 476, 232
- [31] Narayan R., Paczyński B., Piran T., 1992, *Astrophysical Journal* 395, L83
- [32] Paczyński B., *Astrophysical Journal* 494, L45
- [33] Palmer J., Davenhall A.C., June 1999, SC/6.3 The CCD Photometric Calibration Cookbook, Starlink Project, Rutherford Appleton Laboratory
- [34] PixelVision CCD Camera Manual
- [35] Prosper H.B., Spring 1999, Recent Advances in Astronomy and Cosmology Class Notes, Florida State University
- [36] Rees M.J., Mészáros P., 1992, *Montly Notices of the Royal Astronomical Society* 258, P41
- [37] Rhie, S. *et. al.* 2000, *International Astronomical Union Symposium*, 202E
- [38] Rromanishin W., *An Introduction to Astronomical Photometry using CCD's*, University of Oklahoma, 2002
- [39] Stoy R.H., *Precision Photometry*, pp. 8-17, SAAO, 2-3 February 1993, Kilkenny D., Lastovica E., Menzies J.W. (eds.)
- [40] Verbunt F., 1993, *Annual Review of Astronomy and Astrophysics*, 31:93-127
- [41] Warren-Smith R.F., 1998, SUN/33.6 NDF-Routines for Accessing the extensible N-Dimensional Data Format, Starlink Project, Rutherford Appleton Laboratory

- [42] Woosley S., 1993, *Astrophysical Journal* 405, 273
- [43] Young A.T., *Precision Photometry*, pp. 25-34, SAAO, 2-3 February 1993,
Kilkenny D., Lastovica E., Menzies J.W. (eds.)
- [44] Zissell R.E., 1998, *Journal of the American Association of the Variable Star
Observers*, Volume 26, 151
- [45] Zwicky, 1937 *Physical Reviews*, 51, 290

Appendix A

Binary Evolution: Spin-up, spin-down and non-thermal emission from compact objects

Published in: African Skies, May 2002, No 7, 2

J.J. Calitz & P.J. Meintjes

*Department of Physics and Boyden Observatory, University of the Free State, Bloemfontein,
South Africa*

Abstract

The spin-up or spin-down of accreting objects can be used as a diagnostic tool to investigate the mass transfer mechanism between the primary and the secondary stars in binary systems, as well as the evolution of the system. This can place tight constraints on the non-thermal and thermal emission in the system. By getting a global view of the system, potential non-thermal emitters can be identified for future studies with HESS and other new-generation gamma-ray telescopes.

A.1 Introduction

Close binaries are stars locked in orbit around each other, where one star is a compact object with a strong magnetic field and the other star a star that fills its Roche lobe, resulting in an exchange of matter between the two stars. This may lead to a spin-up or spin-down of the compact object, depending on various factors, such as mass transfer rate and mass accretion rate. By looking at mass transfer and mass accretion separately, a better understanding of a system can be reached and prospects for the expectation of flares can be set. The importance of magnetic reconnection and acceleration mechanisms is outlined.

A.1.1 Mass transfer vs. mass accretion

Our approach is to distinguish specifically between mass transfer from the secondary star and mass accretion by the compact (primary) object. Mass transfer is determined by Roche lobe overflow as well as mass loss in the form of stellar wind. Due to the basic structure of the Roche lobe, a maximum mass transfer from the secondary star can be estimated for a lobe filling star, e.g.

$$\dot{M}_2 \simeq 6.4 \times 10^{17} \left(\frac{\rho_{L1}}{\rho_{phot}} \right) \left(\frac{T}{3500 \text{ K}} \right)^{3/2} \left(\frac{P_{orb}}{2h} \right)^2 \text{ g s}^{-1}$$

and the instantaneous mass transfer due to angular momentum losses by (Frank, King & Raine 1992)

$$\dot{M}_2 = M_2 \left(\frac{\dot{J}/J}{4/3 - q} \right)$$

where $q = M_2/M_1$ and \dot{J}/J the sum of angular momentum losses due to gravitational radiation, magnetic braking and other angular momentum losses from the primary and secondary.

The evolution of the binary system is very closely linked to the mass transfer and angular momentum loss history of the system as has been shown (e.g. Meintjes 2001, these proceedings) High mass transfer may lead to the development of an accretion disc, which can spin the compact object up or down, depending on the nature of the interaction of the magnetosphere of the compact object with the disc.

Matter that leaves the L_1 point will lose energy, but not angular momentum as it follows a ballistic trajectory in the orbital plane. It will interact with itself and settle in an accretion ring where the specific angular momentum of the gas is the same as it was at the L_1 point. This ring will spread under viscosity, removing angular momentum from the gas as it moves closer to the compact object. Interaction of the disc with the magnetosphere may lead to a net spin-up or spin-down torque that is exerted on the rotating compact object. (Gosh & Lamb 1979, Wang 1987).

Mass accretion will only take place if matter in the disc, or stellar wind (Bondi-Hoyle type accretion) loses angular momentum, and if the compact star rotates slowly enough to allow accretion instead of centrifugally expelling the gas from the magnetosphere. Important to notice is that the mass transferred from the secondary is not necessarily the mass accreted by the compact object. In general, only a fraction of the transferred material $\dot{M}_1 = -\beta\dot{M}_2$ will be accreted. The fraction lost by the system carries away a fraction α of the angular momentum of the mass losing star. An expression for the binary separation evolution is given by

$$\frac{\dot{a}}{a} = 2 \frac{\dot{J}}{J} + 2 \frac{-\dot{M}_2}{M_2} \left[1 - \frac{\beta M_2}{M_1} \frac{(1-\beta)M_2}{2(M_1 + M_2)} - \frac{\alpha(1-\beta)M_1}{M_1 + M_2} \right].$$

The change in binary separation will influence the Roche lobe dynamics, resulting in a changing of the Roche lobe radius (R_L)

$$\frac{\dot{R}_L}{R_L} = \frac{\dot{a}}{a} + \frac{\dot{M}_2}{3M_2} - \frac{1}{3} \frac{(1-\beta)\dot{M}_2}{M_1 + M_2}.$$

By treating the secondary as a polytrope of index n (King 1988) stars with radiative and convective

envelopes have an adiabatic indexes $\eta_{ad} > 0$ (radiative) and $\eta_{ad} < 0$ (convective) respectively. Therefore, the response of the secondary to mass transfer is determined by

$$\frac{\dot{R}_2}{R_2} = -\eta_{ad} \left(\frac{-\dot{M}_2}{M_2} \right)$$

leading to

$$\begin{aligned} \frac{\dot{R}_2}{R_2} &< 0 \text{ for } \frac{-\dot{M}_2}{M_2} > 0 \text{ (radiative)} \\ \frac{\dot{R}_2}{R_2} &> 0 \text{ for } \frac{-\dot{M}_2}{M_2} > 0 \text{ (convective)} \end{aligned}$$

The reason for this behavior is that stars with convective envelopes have constant entropy profiles throughout the envelope, while stars with radiative envelopes have a steep entropy gradient near the surface. By losing the surface layers when mass is transferred stars with radiative and convective envelopes shrink and expand respectively as a result of the readjustment of the hydrostatic equilibrium (King 1988). It can be shown that constant mass accretion can proceed if the Roche lobe of the secondary expands or contracts with the secondary:

$$\frac{\dot{R}_{2L}}{R_{2L}} = \eta_{ad} \frac{\dot{M}_2}{M_2} = \frac{\dot{a}}{a} + \frac{1}{3} \frac{\dot{M}_2}{M_2} - \frac{1}{3} \frac{(1-\beta)\dot{M}_2}{M_1 + M_2}$$

By using the expression for $\frac{\dot{a}}{a}$, one can show that

$$\frac{\dot{M}_2}{M_2} = \frac{\dot{J}_b/J_b}{\frac{5}{6} + \frac{\eta}{2} - \frac{\beta}{M_1} \frac{M_2}{M_1} - \frac{1}{3} \frac{(1-\beta)M_2}{(M_1+M_2)} - \alpha(1-\beta) \frac{M_1}{M_1+M_2}}.$$

Stable mass transfer can proceed if

$$\frac{5}{6} + \frac{\eta_{ad}}{2} - \frac{\beta}{M_1} \frac{M_2}{M_1} - \frac{1}{3} \frac{(1-\beta)M_2}{(M_1+M_2)} - \alpha(1-\beta) \frac{M_1}{M_1+M_2} > 0$$

which in fact determines the whole evolution of the binary system.

A.2 Star-disc interaction: spin-up and spin-down

The effect that the accretion disc will have on the rotating compact object is implicitly determined by the mass transfer rate and the magnetic field strength of the compact object. As a first approximation spin-up or spin-down of the compact object will occur if the disc-magnetosphere interaction occurs inside or outside the co-rotation radius respectively. This is qualitatively expressed in terms of the fastness parameter, defined by

$$\omega = \frac{\Omega_\star}{\Omega_K(R_m)} = \left(\frac{R_m}{R_c} \right)^{3/2}$$

which gives us a way to indicate the possibility of accretion on the poles of the compact object. Values of $\omega < 1$ indicate a slow rotator where the speed of the compact object is below the Keplerian speed of the gas of the inner disc radius. The rotation is thus slow enough for plasma from the disc to flow to the surface of the star after a sufficient loss of angular momentum. With $\omega \geq 1$ the

star is rotating too fast for matter to get on the magnetic field lines effectively, and is centrifugally expelled from the system. This is known as the *propeller effect*. Therefore, during the propeller phase a lower x-ray flux can be expected resulting from lower mass accretion onto the poles. In this phase thermal emission from the system may shut down significantly, but a significant non-thermal component of the luminosity may be possible due to the energy release $-\dot{E} = I\Omega\dot{\Omega}$ as a result of the spin-down of the compact object. However, this may be of transient nature, like reported for the nova like variable AE Aquarii which is also in a propeller phase (Meintjes & de Jager, 2000 and references therein).

The equilibrium period (P_{eq}) is defined as the period when the period of the compact star rotation is approximately equal to the rotation rate of the disc's inner edge, which is at the co-rotation radius, i.e. when $\omega = 1$,

$$P_{eq} \approx 3M_1^{-5/7} \dot{M}_{17}^{-3/7} \mu_{30}^{6/7} \text{ sec.}$$

This estimate of the equilibrium period can now be used to evaluate individual sources. Sources that are "out of equilibrium" are in a spin-up or spin-down phase, which imply that differential rotation exists between the compact object and certain parts of the disc. This provides an opportunity for the development and amplification of azimuthal magnetic fields that may build up to flares, which in turn may result in the release of significant energy fluxes in relativistic particles and resultant γ -emission. The dominant mechanism in the triggering of the flares is magnetic reconnection.

A.3 Magnetospheric flares

Aly & Kuijpers (1991) showed that the energy stored in the sheared flux tubes caused by the differential rotation between the compact object and the disc that may be released in a reconnection process is $W_m \simeq B_\phi^2(R)l^2R/8\pi$ where B_ϕ is the azimuthal magnetic field at a distance R , determined by

$$B_\phi = B_p \Delta\phi (1 - 6.7 \times 10^{-3} P_\star^{-2/3} M_1^{-1/3} \omega^{-2/3})^{-1/2}$$

and l is the distance between flux tubes. The maximum available luminosity will be given by

$$\begin{aligned} L &\approx W_m \Omega_B \\ &= W_m (\Omega_K(R) - \Omega_\star) \\ &= 1.3 \times 10^{35} B_{\star 10}^2 R_{\star 6}^6 R_7^{-4} l_6^2 \left[\frac{\Omega_B}{200\text{Hz}} \right] \text{ erg s}^{-1} \end{aligned}$$

These bursts may thus occur on average with the beat frequency of the system if the magnetic field is amplified enough. These reconnections can possibly explain the quasi periodic oscillations in some LMXRB's. Non-thermal outbursts reported from the enigmatic nova-like variable AE Aqr may also be produced in a similar mechanism (Meintjes & de Jager, 2000).

The energy released in these magnetosphere flares may, through mechanisms like shocks, current dissipation in reconnection events and double-layers produce copious fluxes of relativistic particles in transient burst-like events. If it is assumed that particles are accelerated to relativistic energies

from a more or less thermal population, the resultant spectrum may be

$$\frac{dN}{dE} = N_p (k_B T_m) E^{-2} \text{ cm}^{-3} \text{ erg}^{-1}$$

where N_p and T_m represents the particle density and magnetosphere temperature respectively (Meintjes & Kanbach, 1994). The resultant γ -ray flux produced through π^0 decays the relativistic particles interact with the target matter as

$$F_\gamma = \frac{8\pi}{3} N_p^2 D^{-2} (k_B T_m) E^{-1} R_m^3 <\sigma> c P_{esc}$$

where $<\sigma>$ is the cross section for $p-p$ collisions and $P_{esc} = 1 - N_p \sigma R_m$ is the escape probability for a γ -ray produced in this process.

A.4 Observational issues

In the propeller phase we expect low accretion on to the polar caps of the rotating compact object, with an accompanying decrease in the thermal, accretion induced, emission from the system. However, during this phase the system may become a transient non-thermal emitter. Using our model, we expect to make a useful system analysis, so that the probability of expecting activity from these systems can be estimated. Sources both in and out of equilibrium is currently investigated.

To estimate the visibility of the flares for Cerenkov telescopes, we used the values $N_p \sim 10^{15} \text{ cm}^{-3}$, $T_s \sim 10^{10} \text{ K}$, $\sigma \sim 10^{-27}$, $R_m \sim 10^8 \text{ cm}$, and $P_{esc} \sim 0.9$. At a distance of 1 kpc, an upper limit for the expected burst fluxes for energies of the order of 10^3 GeV can be of the order of $\leq 10^{-9} \text{ ph cm}^{-2} \text{ s}^{-1}$, which is much higher than the expected detection threshold of $10^{-13} \text{ ph cm}^{-2} \text{ s}^{-1}$ (above 1 TeV) of the HESS Cerenkov detector which is currently under construction in Namibia. Although this estimate is an upper limit, we hope it would stimulate the interest of the high energy community to include these type of sources in future observational campaigns.

A.5 Conclusion

These results are preliminary. In the above approach we assumed steady mass transfer and angular momentum effects only. The purpose of this study is to point out the relevance of star-disc interactions for the production of TeV flares from accreting compact objects for future Cerenkov telescopes. By improving our understanding of magnetospheric processes in accreting systems, more realistic predictions regarding VHE emission can be made. A more detailed, in depth, study of these processes is currently in progress.

Bibliography

- [1] Aly J.J., Kuijpers J., 1990, A&A, 227:473-482
- [2] Frank J., King A.R., Raine D.J., 1992, Accretion Power in Astrophysics, 2nd ed., Cambridge University Press
- [3] Gosh P., Lamb F.K., 1979a, ApJ. 232, 259
- [4] Gosh P., Lamb F.K., 1979b, ApJ. 234, 296
- [5] King A.R., 1988, Q. Jl. R. astr. Soc., 29, 1-25
- [6] Lamb, F.K., 1989, Timing Neutron Stars, Kluwer Academic Publishers Astrophys., 22:537-592
- [7] Meintjes P.J., Kanbach G., 1994, Currents in High-Energy Astrophysics, 31-38, Kluwer Academic Publishers
- [8] Meintjes P.J., de Jager O.C., 2000, Mon.Not.R.Astron. Soc., 311, 611-620
- [9] Meintjes P.J., 2002, Afr.Sk., May, 7, 5
- [10] Wang Y.-M., 1987, Astron. Astrophys, 183, 257